

Quantum Error Mitigation via Quantum-Noise-Effect Circuit Groups

Yusuke Hama¹ and Hirofumi Nishi^{2,1}

¹*Quemix Inc., 2-11-2 Nihombashi, Chuo-ku, Tokyo 103-0027, Japan*

²*Laboratory for Materials and Structures, Institute of Innovative Research,
Tokyo Institute of Technology, Yokohama 226-8503, Japan*

(Dated: May 30, 2022)

Our near-term quantum computers have been built as intermediate-scale quantum devices and are fragile against quantum noise effects, namely, NISQ devices. Traditional quantum-error-correcting (QEC) codes are not implemented on such devices and to perform quantum computation in good accuracy with these machines we need to develop alternative approaches for mitigating quantum computational errors. In this work, we propose quantum error mitigation (QEM) scheme for quantum computational errors which occur due to couplings with environments during gate operations, i.e., decoherence. To establish our QEM scheme, first we estimate the quantum noise effects on single-qubit states and represent them as groups of quantum circuits, namely, quantum-noise-effect circuit groups. Then our QEM scheme is conducted by subtracting expectation values generated by the quantum-noise-effect circuit groups from that obtained by the quantum circuit for the quantum algorithm under consideration. As a result, the quantum noise effect is reduced, and we obtain approximately the ideal expectation values via the quantum-noise-effect circuit group and the number of elementary quantum circuits composing it scales polynomial with respect to the product of the depth of quantum algorithm and the number of register bits. To numerically demonstrate the validity of our QEM scheme, we run noisy quantum simulations of qubits under the amplitude damping (AD) effects for four types of quantum algorithms. Our QEM scheme is solely composed of quantum-computational operations (quantum gates and measurements), and thus, it can be conducted by any type of quantum device without having limitations on the number of register bits and error rates of quantum gates. In addition, it can be applied to error mitigation for many other types of quantum noise effects as well as noisy quantum computing of long-depth quantum algorithms.

I. INTRODUCTION

The research and development of quantum computers are currently an important and active field of quantum information science and technology [1–12]. On the one side, quantum computer devices have been engineered with state-of-the-art technologies using various kinds of elements including superconducting circuits [7–10, 13–16] and trapped ions [11, 12, 17–21]. On the other side, toward the application to, for example, material science, quantum chemistry, optimization problems, and quantum machine learning, many new kinds of quantum algorithms have been recently developed such as Variational Quantum Eigensolver (VQE) [22–26], Quantum Approximate Optimization Algorithm (QAOA) [26–32], and quantum circuit learning [26, 33–35]. These algorithms have characteristics such that they are constructed by the hybridization between quantum and classical computational procedures. Recently, in the task of sampling random quantum circuits, quantum supremacy has been demonstrated using the superconducting circuit device [36]. All these facts are implying important milestones for the advancement of the research and development of the quantum computers and the broadening of quantum-computing applications to many fields of science and engineering.

While the above successful results of the research and development of quantum computers have been reported, our near-term quantum computers based on circuit models have been built as intermediate-scale quantum devices yet and are fragile against quantum noise effects: they are called NISQ devices [9, 11, 37]. Quantum noise effects (decoherence) are major obstacles for performing quantum computation and historically many great efforts have been made on reducing

such effects [38, 39]. One of the traditional and representative schemes for this are the quantum-error-correction (QEC) coding [5, 9, 10, 16, 40–43]. Another important one is the dynamical decoupling which plays fundamental role in extending coherence times of qubits [8, 11, 16, 42, 44–47]. The QEC codes are, however, not implemented on NISQ devices and to obtain quantum computational results in good accuracy with NISQ devices we need to search for alternative approaches for mitigating quantum noise effects. This research field is called quantum error mitigation (QEM), and these days, it is one of the important themes of the research and development of quantum computation [25, 26, 48–64]. The difficulty of the treatment of quantum noises (e.g., amplitude damping, phase damping (dephasing), depolarizing channel) is that we cannot directly construct their inverse processes by quantum gates due to their non-unitarity. On the other hand, it is possible to formulate quantum noise effects as quantum circuits by using ancilla bits and measurements on them [5, 65–71]. By utilizing the quantum circuits representing the quantum noise effects under consideration, we expect that we can establish QEM schemes for reducing such effects. If this is established, we become able to mitigate the quantum noise effects by the gate operations and measurements, i.e., QEM conducted by all-quantum-computational operations. In other words, we become able to programmably run quantum algorithms with mitigating the quantum noise effects solely by the quantum computational operations and realize high-accurate quantum computation.

In this work, we propose our QEM schemes for quantum computational errors which occur owing to couplings with environments (decoherence) during gate operations: errors of state preparation (initialization) and measurement, imperfect

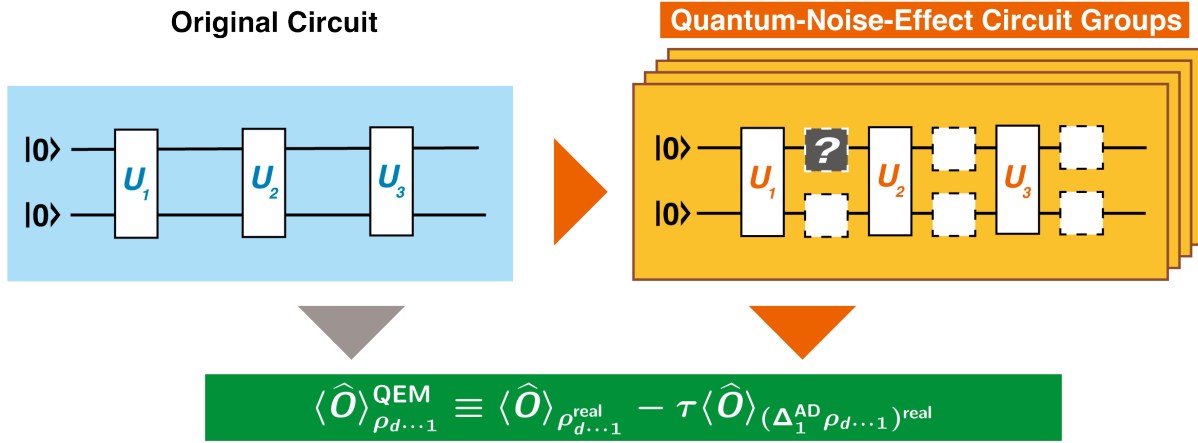


FIG. 1. Schematic of our proposed QEM method. The original circuit represented by the blue rectangle (left side) describes the quantum circuit for the quantum algorithm to be ran and is composed of the unitary operations U_k with $k = 1, \dots, d$ and d denotes the depth of the quantum algorithm. It yields the expectation value $\langle \hat{O} \rangle_{\rho_{d \dots 1}}^{\text{real}}$. On the other hand, the quantum-noise-effect circuit group, which is represented by the orange rectangles (right side), is constructed from the original circuit by inserting an additional operation between U_k and U_{k+1} (gray box). It yields the theoretically-estimated quantum computational error $\langle \hat{O} \rangle_{(\Delta_1^{\text{AD}} \rho_{d \dots 1})}^{\text{real}}$. By using these two expectation values, we obtain the equation for our QEM scheme in the green rectangle. Here we have taken $d = 3$.

tions of quantum gates, and cross talks among qubits are not taken into account. In particular, we make detailed analysis on quantum computational errors generated by amplitude damping (AD) of single-qubit states. We show the schematic representation of our QEM scheme in Fig. 1 and it consists of two elements, the quantum circuit for the quantum algorithm under consideration (original circuit) represented by the blue rectangle and the ensemble of quantum circuits which yields the theoretical value of the quantum computational error due to the quantum noise effect, namely, quantum-noise-effect circuit group and is represented by the orange rectangles. By utilizing the quantum-noise-effect circuit group, we formulate our QEM scheme as a perturbation theory with respect to a strength of quantum noise and perform it by subtracting the expectation values given by the quantum-noise-effect circuit groups from the those generated by the quantum circuit for the quantum algorithms under consideration as expressed by the formula in the green rectangle; see also the right-hand side of the first line in Eq. (8). As a result, the AD effects are mitigated and we approximately obtain the ideal expectation values. Then, we discuss the number of elementary quantum circuits which compose the quantum-noise-effect circuit group and show that it scales polynomial (linear) with respect to the product of the number of register bits and the depth of quantum algorithm (circuit depth or the number of unitary gates composing the quantum algorithm). Finally, we numerically demonstrate the validity of our QEM scheme by running noisy quantum simulators of qubits under the AD effects for four types of quantum algorithms in the linear-order perturbation regime. The detailed explanation on how to extend our QEM scheme to other kinds of quantum noise effects including phase damping, generalized amplitude damping (thermalization), and depolarizing channel, and extension of our QEM

scheme to higher-order quantum noise effects are given in appendix.

The structure of this paper is given as follows. It begins by Sec. II with our modeling of the quantum computation under the influence of the quantum noise effect. After then we explain the formalisms of our QEM scheme. In Sec. III, which presents our main results, we demonstrate numerically our QEM schemes for the noisy quantum simulations for four types of quantum algorithms. Sec. IV is devoted to the conclusion of this paper.

II. QEM SCHEMES

A. Modeling and Formulation

Let us explain our modeling of quantum computation under the influence of quantum noise effects. In the following, we focus on the amplitude damping (AD) effect: generalized-amplitude-damping (GAD) effect at zero temperature. As discussed later, it is straightforward to generalize the argument for the AD effect to other quantum noise effects such as phase damping (PD) and stochastic Pauli noises. We schematically represent such a circumstance as a quantum circuit and show it in Fig. 2. There are N_q register bits and the quantum algorithm to be run is represented by the unitary transformation U^{QC} . It is comprised of d unitary transformations described by $U^{\text{QC}} = \prod_{k=1}^d U_k = U_d \cdot U_{d-1} \cdots U_2 \cdot U_1$. The unitary transformation U_k ($k = 1, 2, \dots, d$) is composed of single- and two-qubit gates. We assume that the duration time (gate operation time) of the unitary transformation U_k is Δt for any k . During the time interval Δt , the register bits are influenced by the AD effects due to couplings with environments, e.g.,

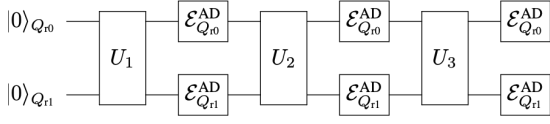


FIG. 2. Illustration of quantum computation under AD effects represented as a quantum circuit. Here we show it for $d = 3$ and $N_q = 2$. The symbol $\mathcal{E}_{Q_{rj}}^{AD}$ expresses the occurrence of AD effect on the register bit Q_{rj} (the j -th register bit).

electromagnetic field in the vacuum, phonons in solids, etc. The quantum master equation describing the AD process in the interaction picture is given by [5, 72–74]

$$\begin{aligned} \frac{\partial \rho(t)}{\partial t} &= \gamma \mathcal{L}_{AD}[\rho(t)] \\ &= \gamma \sum_{j=0}^{N_q-1} \left[\tilde{\sigma}_j^- \rho(t) \tilde{\sigma}_j^+ - \frac{1}{2} \{ \tilde{\sigma}_j^+ \tilde{\sigma}_j^-, \rho(t) \} \right], \quad (1) \end{aligned}$$

where $\rho(t)$ is the density matrix of the N_q register bits at a time t and γ is the decay rate. The symbol \mathcal{L}_{AD} denotes the Lindblad superoperator of the AD process and the operators $\tilde{\sigma}_j^\pm = \frac{X_j \mp i Y_j}{2}$ are the ladder (raising and lowering) operators acting on the register bit Q_{rj} . X_j and Y_j are X and Y gates acting on Q_{rj} , respectively. $\{A, B\}$ is the anti-commutator between the operators A and B . In our model, we assume that the N_q register bits experience homogeneously the AD effect of single-qubit state given by the decay rate γ . At the initial time $t = 0$, all the register bits are in $|0\rangle$ state (ground state), namely, $\rho(0) = |0\rangle\langle 0|^{\otimes N_q}$. Let us write the total amount of quantum computational time (running time of the quantum algorithm under consideration) by $T (= d \cdot \Delta t)$ while we introduce the dimensionless time $\tau = \gamma \Delta t$. By assuming $\tau \ll 1$, in the following let us evaluate the density matrix at the time T , $\rho(T)$, by using the quantum master equation (1) and express it as a perturbation series with respect to τ given by

$$\begin{aligned} \rho(T) &= \sum_{p=0}^{\infty} \frac{\tau^p}{p!} \cdot \Delta_p^{AD} \rho_{d \dots 1} \\ &= \rho_{d \dots 1} + \tau \cdot \Delta_1^{AD} \rho_{d \dots 1} + \mathcal{O}(\tau^2). \quad (2) \end{aligned}$$

Here $\rho_{d \dots 1} = U^{QC} \cdot \rho(0) \cdot (U^{QC})^\dagger$ describes the noise-free (ideal) quantum state of the register bits. In other words, it is the ideal output quantum state generated by the quantum algorithm given by U^{QC} . The quantity $\Delta_p^{AD} \rho_{d \dots 1}$ ($p \geq 1$) is the theoretically-evaluated p -th-order AD effect. Let us focus on the first-order AD effect $\Delta_1^{AD} \rho_{d \dots 1}$ which has the form

$$\begin{aligned} \Delta_1^{AD} \rho_{d \dots 1} &= \sum_{k=1}^d \Delta_{1,k}^{AD} \rho_{d \dots 1}, \\ \Delta_{1,k}^{AD} \rho_{d \dots 1} &= \left(\prod_{l=k+1}^d U_l \right) \cdot \tilde{\rho}_{k \dots 1}^{AD} \cdot \left(\prod_{l=k+1}^d U_l \right)^\dagger, \quad (3) \end{aligned}$$

where

$$\begin{aligned} \tilde{\rho}_{k \dots 1}^{AD} &= \mathcal{L}_{AD}[\rho_{k \dots 1}] = \sum_{j=0}^{N_q-1} \left[\tilde{\sigma}_j^- \rho_{k \dots 1} \tilde{\sigma}_j^+ - \frac{1}{2} \{ P_j^1, \rho_{k \dots 1} \} \right], \\ \rho_{k \dots 1} &= \left(\prod_{l=1}^k U_l \right) \cdot \rho(0) \cdot \left(\prod_{l=1}^k U_l \right)^\dagger, \quad (4) \end{aligned}$$

with $\prod_{l=k+1}^d U_l = U_d \cdot U_{d-1} \cdots U_{k+2} \cdot U_{k+1}$ and $\prod_{l=1}^k U_l = U_k \cdot U_{k-1} \cdots U_2 \cdot U_1$. The operator $P_j^1 = \tilde{\sigma}_j^+ \tilde{\sigma}_j^- = \frac{1_j - Z_j}{2}$ describes the projection onto the quantum state $|1\rangle_j$ with 1_j and Z_j denoting the identity operator and the Z gate acting on Q_{rj} , respectively: On the other hand, the projection operator of the quantum state $|0\rangle_j$ is given by $P_j^0 = \tilde{\sigma}_j^- \tilde{\sigma}_j^+ = \frac{1_j + Z_j}{2}$.

B. QEM Scheme

Since we have evaluated the single-qubit-state AD effect, next we discuss our quantum error mitigation (QEM) scheme. We denote the operator of which we are aiming to take an expectation value by \hat{O} . When we implement the quantum state ρ on a real device what we actually obtain is a quantum state which is different from ρ due to quantum noise effects: Note again that hereinafter we only consider the AD effect. Let us write it by ρ^{real} . We represent the density matrix ρ^{real} in terms of ρ (ideal state) as $\rho^{\text{real}} = \rho + \delta^{\text{AD}} \rho$, where $\delta^{\text{AD}} \rho$ represents the deviation from ρ owing to the AD effect on a real device. Note that we use the symbol δ^{AD} to describe the AD effect on a real device while we use Δ^{AD} to describe the theoretically-estimated AD effect like Eq. (2). Namely, a quantum computational error occurs due to the deviation $\delta^{\text{AD}} \rho$. QEM is a prescription for mitigating the error coming from the deviation $\delta^{\text{AD}} \rho$. Mathematically, this is a task to make the value of $\text{Tr}(\hat{O} \delta^{\text{AD}} \rho)$ as small as possible. In our scheme, we mitigate the error $\text{Tr}(\hat{O} \delta^{\text{AD}} \rho)$ by perturbatively treating the deviation $\delta^{\text{AD}} \rho$ with respect to τ and using the theoretically-estimated AD effect $\Delta_p^{\text{AD}} \rho$. In the following we show such a perturbative analysis up to the first order in τ . The extension of QEM scheme to higher-order AD effect is discussed in Appendix. **A1.** The key procedure of our QEM scheme is to construct quantum circuits for computing the quantity $\text{Tr}(\hat{O} \Delta_1^{\text{AD}} \rho_{d \dots 1})$, which describes the theoretically-estimated quantum computational error of the expectation value $\text{Tr}(\hat{O} \rho)$ in the first order of τ . For doing this, there are two difficulties: (i) the generation of the anti-commutator term $\{P_j^1, \rho_{k \dots 1}\}$ in Eq. (4) and (ii) the implementation of the non-unitary operators $\tilde{\sigma}_j^-$ and P_j^1 . Let us discuss from our solution to the difficulty (i). We denote some sort of quantum-computational operation (gate operation or measurement) by \mathcal{A} . When the operation \mathcal{A} acts on the quantum state $\rho_{k \dots 1}$ the output state we have is $\rho_{k \dots 1} \rightarrow \mathcal{A} \rho_{k \dots 1} \mathcal{A}^\dagger$. The anti-commutator term $\{P_j^1, \rho_{k \dots 1}\}$, in contrast, is not represented in this way, and thus, it is not clear how to generate such a term by the quantum-computational operations. We solve this in the following way. To make our argument simple, here let focus on

the single-register-bit system ($N_q = 1$); the generalization to $N_q \geq 2$ is straightforward and is discussed later. First, we rewrite $\tilde{\rho}_{k\dots 1}^{\text{AD}}$ in Eq. (4) as

$$\tilde{\rho}_{k\dots 1}^{\text{AD}} = -\frac{\rho_{k\dots 1}}{4} + \frac{Z\rho_{k\dots 1}Z}{4} + \tilde{\sigma}^- \rho_{k\dots 1} \tilde{\sigma}^+ - P^1 \rho_{k\dots 1} P^1. \quad (5)$$

In the above way, all the four terms in Eq. (5) are written in the form $\mathcal{A}\rho_{k\dots 1}\mathcal{A}^\dagger$, and thus, we have solved the difficulty (i). Let us analyze the mathematical structure of the right-hand side of Eq. (5). The quantum circuit for creating the first term is straightforward because it is obtained by the quantum circuit composed of U^{QC} (the quantum algorithm under consideration). The implementation of the quantum circuit for the second term $\frac{Z\rho_{k\dots 1}Z}{4}$ is also straightforward because we just apply the Z gate after the operation of U_k . The unclear part is to find ways to construct the quantum circuits for generating the third and fourth terms given by the non-unitary operators $\tilde{\sigma}^-$ and P^1 and this is nothing but the difficulty (ii). We solve this by using an ancilla bit and a measurement on it [5]. For the creating the operation $\tilde{\sigma}^-$, we use the quantum circuit presented in Fig. 3 (a) (AD-effect circuit A) while for the operation of P^1 we use the one in Fig. 3 (b) (AD-effect circuit B). In

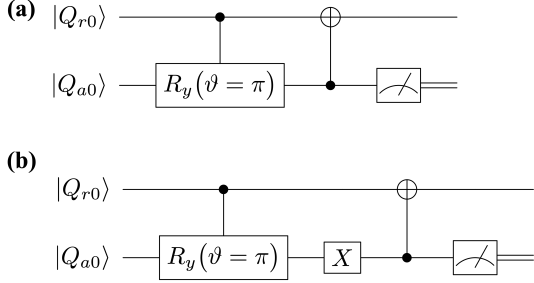


FIG. 3. (a) Schematic of AD-effect circuit A. When we set $\vartheta = \pi$ and post-select the measurement result of the quantum state of Q_{a0} to be $|1\rangle_{Q_{a0}}$, we realize the operation of $\tilde{\sigma}^-$ on Q_{r0} . (b) Schematic of AD-effect circuit B. By setting $\vartheta = \pi$ and post-selecting the measurement result of the quantum state of Q_{a0} to be $|0\rangle_{Q_{a0}}$, we realize the operation of P^1 on Q_{r0} .

both quantum circuits, we regard the ancilla bit Q_{a0} as the environment which induces the AD effect on the register bit Q_{r0} . The interactions between these two qubits are represented by the controlled-rotational gate $U_{CR_y}[Q_{r0}; Q_{a0}](\vartheta)$ and the controlled-not gate $U_{CX}[Q_{a0}; Q_{r0}]$. The controlled-rotational gate $U_{CR_y}[Q_{r0}; Q_{a0}](\vartheta)$ describes the rotation about y axis

by the rotational angle ϑ and it is composed of the control bit Q_{r0} and the target bit Q_{a0} . On the other hand, for the gate operation $U_{CX}[Q_{a0}; Q_{r0}]$ the ancilla bit Q_{a0} is the control bit while the register bit Q_{r0} is the target bit. We have used the notation such that the control bit(s) comes before the semicolon while the target bit(s) comes after. Let us explain the output states generated by the AD-effect circuits A and B. For both quantum circuits, the initial quantum states of Q_{r0} and Q_{a0} are the same and it is $\rho_{Q_{r0}Q_{a0}}(0) = \rho_{Q_{r0}}(0) \otimes \rho_{Q_{a0}}(0)$ with $\rho_{Q_{r0}}(0) = |0\rangle_{Q_{r0}}\langle 0|$ and $\rho_{Q_{a0}}(0) = |0\rangle_{Q_{a0}}\langle 0|$. The AD-effect circuit A is given by the unitary operation $U_{\text{ADA}} = U_{CX}[Q_{a0}; Q_{r0}] \cdot U_{CR_y}[Q_{r0}; Q_{a0}](\vartheta)$ while the AD-effect circuit B is given by $U_{\text{ADB}} = U_{CX}[Q_{a0}; Q_{r0}] \cdot (\mathbf{1}_{2 \times 2} \otimes X_{Q_{a0}}) \cdot U_{CR_y}[Q_{r0}; Q_{a0}](\vartheta)$, where $\mathbf{1}_{2 \times 2}$ is the two by two identity operator. Owing to these unitary operations, the quantum state generated by the AD-effect circuit A is given by $\rho_{\text{ADA}, Q_{r0}Q_{a0}}(\vartheta) = U_{\text{ADA}} \cdot \rho_{Q_{r0}Q_{a0}}(0) \cdot (U_{\text{ADA}})^\dagger$ while the quantum state created by the AD-effect circuit B is $\rho_{\text{ADB}, Q_{r0}Q_{a0}}(\vartheta) = U_{\text{ADB}} \cdot \rho_{Q_{r0}Q_{a0}}(0) \cdot (U_{\text{ADB}})^\dagger$. At the end, we measure the ancilla bit Q_{a0} . Then the quantum states of Q_{r0} (reduced density matrices) are described by the Kraus operators [5, 75].

$$\begin{aligned} \mathcal{K}_0^{\text{ADA}} &= {}_{Q_{a0}}\langle 0|U_{\text{ADA}}|0\rangle_{Q_{a0}} = P^0 + \cos\left(\frac{\vartheta}{2}\right) P^1 \\ \mathcal{K}_1^{\text{ADA}} &= {}_{Q_{a0}}\langle 1|U_{\text{ADA}}|0\rangle_{Q_{a0}} = \sin\left(\frac{\vartheta}{2}\right) \tilde{\sigma}^-, \\ \mathcal{K}_0^{\text{ADB}} &= {}_{Q_{a0}}\langle 0|U_{\text{ADB}}|0\rangle_{Q_{a0}} = \sin\left(\frac{\vartheta}{2}\right) P^1, \\ \mathcal{K}_1^{\text{ADB}} &= {}_{Q_{a0}}\langle 1|U_{\text{ADB}}|0\rangle_{Q_{a0}} = \tilde{\sigma}^+ + \cos\left(\frac{\vartheta}{2}\right) \tilde{\sigma}^-. \end{aligned} \quad (6)$$

For the AD-effect circuit A (B) the Kraus operators $\mathcal{K}_0^{\text{ADA}}$ ($\mathcal{K}_0^{\text{ADB}}$) acts on the register bit Q_{r0} when the measurement outcome of the quantum state of the ancilla bit Q_{a0} is $|0\rangle_{Q_{a0}}$ while $\mathcal{K}_1^{\text{ADA}}$ ($\mathcal{K}_1^{\text{ADB}}$) operates when the measurement outcome is $|1\rangle_{Q_{a0}}$. When we average these two outcomes, the quantum state of Q_{r0} created by the AD-effect circuit A is given by $\rho_{\text{ADA}, Q_{r0}}(\vartheta) = \text{Tr}_{Q_{a0}}[\rho_{\text{ADA}, Q_{r0}Q_{a0}}(\vartheta)] = \sum_{\mu=0,1} \mathcal{K}_\mu^{\text{ADA}} \cdot \rho_{Q_{r0}}(0) \cdot (\mathcal{K}_\mu^{\text{ADA}})^\dagger$, where the symbol $\text{Tr}_{Q_{a0}}$ denotes the partial trace with respect to Q_{a0} degrees of freedom. Similarly, for the AD-effect circuit B we have $\rho_{\text{ADB}, Q_{r0}}(\vartheta) = \sum_{\mu=0,1} \mathcal{K}_\mu^{\text{ADB}} \cdot \rho_{Q_{r0}}(0) \cdot (\mathcal{K}_\mu^{\text{ADB}})^\dagger$. In particular, for the AD-effect circuit A when we take ϑ to be ϑ_t such that $\cos^2\left(\frac{\vartheta_t}{2}\right) = e^{-\gamma t}$ [5], the matrix representation of $\rho_{\text{ADA}, Q_{r0}}(\vartheta_t)$ is given by

$$\rho_{\text{ADA}, Q_{r0}}(\vartheta_t) = \begin{pmatrix} [\rho_{\text{ADA}, Q_{r0}}(0)]_{00} + [\rho_{\text{ADA}, Q_{r0}}(0)]_{11} (1 - e^{-\gamma t}) & [\rho_{\text{ADA}, Q_{r0}}(0)]_{01} e^{-\frac{\gamma t}{2}} \\ [\rho_{\text{ADA}, Q_{r0}}(0)]_{10} \cdot e^{-\frac{\gamma t}{2}} & [\rho_{\text{ADA}, Q_{r0}}(0)]_{11} e^{-\gamma t} \end{pmatrix}. \quad (7)$$

The matrix element $[\rho_{\text{ADA}, Q_{r0}}(0)]_{nn'}$ ($n, n' = 0, 1$) denotes

the (n, n') -element of $\rho_{\text{ADA}, Q_{r0}}(0)$. The reduced density ma-

trix $\rho_{\text{ADA}, Q_{r0}}(\vartheta_t)$ in Eq. (7) is nothing but the solution of the quantum master equation (1). Further, when we take $\vartheta_t \rightarrow \pi$, the Kraus operators in Eq. (6) becomes $\{\mathcal{K}_0^{\text{ADA}}, \mathcal{K}_1^{\text{ADA}}\} \rightarrow \{P^0, \tilde{\sigma}^-\}$, $\{\mathcal{K}_0^{\text{ADB}}, \mathcal{K}_1^{\text{ADB}}\} \rightarrow \{\tilde{\sigma}^+, P^1\}$. Therefore, for the case of the AD-effect circuit A by using the measurement result of Q_{a0} such that we post-select the output state of Q_{a0} to be $|1\rangle_{Q_{a0}}$ we can realize the operation of $\tilde{\sigma}^-$ on Q_{r0} . On the other hand, for the AD-effect circuit B by post-selecting the output state of Q_{a0} to be $|0\rangle_{Q_{a0}}$ we realize the operation of P^1 on Q_{r0} . To show the above things concretely, let us present the examples of the quantum circuits for the generation of $\left(\prod_{l=k+1}^d U_l\right) \cdot (\tilde{\sigma}^- \rho_{k\dots 1} \tilde{\sigma}^+) \cdot \left(\prod_{l=k+1}^d U_l\right)^\dagger$ and $\left(\prod_{l=k+1}^d U_l\right) \cdot (P^1 \rho_{k\dots 1} P^1) \cdot \left(\prod_{l=k+1}^d U_l\right)^\dagger$ for $k = 2, d = 3$, and we show them in Figs. 4 (a) and 4 (b), respectively. As a result, by using the AD-effect circuits A and B we can perform the actions of $\tilde{\sigma}^-$ and P^1 as described by the third and four terms in Eq. (5), and thus, we have solved the second difficulty (ii).

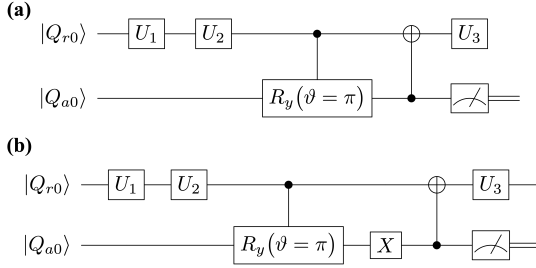


FIG. 4. (a) Schematic of an elementary quantum circuit in the AD-effect circuit group given by the AD-effect circuit A which generates $\left(\prod_{l=k+1}^d U_l\right) \cdot (\tilde{\sigma}^- \rho_{k\dots 1} \tilde{\sigma}^+) \cdot \left(\prod_{l=k+1}^d U_l\right)^\dagger$. For doing so, we set $\vartheta = \pi$ and post-select the measurement result of the quantum state of Q_{a0} to be $|0\rangle_{Q_{a0}}$. (b) Schematic of an elementary quantum circuit in the AD-effect circuit group given by the AD-effect circuit B. When we post-select the measurement outcome of Q_{a0} to be $|1\rangle_{Q_{a0}}$, we have $\left(\prod_{l=k+1}^d U_l\right) \cdot (P^1 \rho_{k\dots 1} P^1) \cdot \left(\prod_{l=k+1}^d U_l\right)^\dagger$. Both of these quantum circuits in (a) and (b) are for $k = 2, d = 3$ with $\vartheta = \pi$.

Since the difficulties (i) and (ii) have been solved, we are now ready to establish our QEM scheme. To compute the quantity $\text{Tr}(\hat{O} \cdot \Delta_1^{\text{AD}} \rho_{d\dots 1})$ we need four types of quantum circuits: the original circuit given by U^{QC} , the quantum circuit where the additional Z gate is performed, and the AD-effect circuits A and B. The latter three quantum-circuit ensembles composed of the additional Z -gate, $\tilde{\sigma}^-$, and P^1 operations form the quantum-noise-effect circuit group for the AD effect, i.e., AD-effect circuit group. Hereinafter, let us write the trace of the product between the operator \hat{O} and ρ by $\text{Tr}(\hat{O}\rho) = \langle \hat{O} \rangle_\rho$. We perturbatively express the quantum states $\rho_{d\dots 1}^{\text{real}}$ with respect to τ as $\rho_{d\dots 1}^{\text{real}} = \rho_{d\dots 1} + \delta^{\text{AD}}(\rho_{d\dots 1})$ with $\delta^{\text{AD}}(\rho_{d\dots 1}) = \sum_{p=1}^{\infty} \frac{\tau^p}{p!} \cdot \delta_p^{\text{AD}}(\rho_{d\dots 1})$. Furthermore, we write the quantity which is obtained by the implementation of $\Delta_1^{\text{AD}} \rho_{d\dots 1}$ on a real device by $(\Delta_1^{\text{AD}} \rho_{d\dots 1})^{\text{real}}$. With similar to $\rho_{d\dots 1}^{\text{real}}$, we perturbatively express $(\Delta_1^{\text{AD}} \rho_{d\dots 1})^{\text{real}}$ in terms of $\Delta_1^{\text{AD}} \rho_{d\dots 1}$

and τ as $(\Delta_1^{\text{AD}} \rho_{d\dots 1})^{\text{real}} = \Delta_1^{\text{AD}} \rho_{d\dots 1} + \delta^{\text{AD}}(\Delta_1^{\text{AD}} \rho_{d\dots 1})$ with $\delta^{\text{AD}}(\Delta_1^{\text{AD}} \rho_{d\dots 1}) = \sum_{p=1}^{\infty} \frac{\tau^p}{p!} \cdot \delta_p^{\text{AD}}(\Delta_1^{\text{AD}} \rho_{d\dots 1})$. Then, by using Eqs. (2), (3), (4), and (5) we obtain the quantum-error-mitigated expectation value of \hat{O} given by

$$\begin{aligned} \langle \hat{O} \rangle_{\rho_{d\dots 1}}^{\text{QEM}} &\equiv \langle \hat{O} \rangle_{\rho_{d\dots 1}^{\text{real}}} - \tau \langle \hat{O} \rangle_{(\Delta_1^{\text{AD}} \rho_{d\dots 1})^{\text{real}}} \\ &= \langle \hat{O} \rangle_{\rho_{d\dots 1}} + \tau \left(\langle \hat{O} \rangle_{\delta_1^{\text{AD}}(\rho_{d\dots 1})} - \langle \hat{O} \rangle_{\Delta_1^{\text{AD}} \rho_{d\dots 1}} \right) \\ &\quad + \mathcal{O}(\tau^2). \end{aligned} \quad (8)$$

The idea of our QEM scheme is clearly represented in the second line of Eq. (8). The first term is the ideal expectation value while the second term represents the conduction of our QEM scheme. It is described as the subtraction between $\langle \hat{O} \rangle_{\delta_1^{\text{AD}}(\rho_{d\dots 1})}$ (the quantum computational error occurring on a real device) and $\langle \hat{O} \rangle_{\Delta_1^{\text{AD}} \rho_{d\dots 1}}$ (theoretically-evaluated quantum computational error), which is computed by the AD-effect circuit group. The heart of the idea for doing this is that we have considered that the real noise effect $\delta_1^{\text{AD}}(\rho_{d\dots 1})$ is (approximately) equivalent to the theoretically-estimated noise effect $\Delta_1^{\text{AD}}(\rho_{d\dots 1})$. When the second term in the second line of Eq. (8) becomes small enough, we consider that we have accomplished in mitigating the error of quantum computation on a real device. Note that the quantum noise effects coming from $\delta^{\text{AD}}(\Delta_1^{\text{AD}} \rho_{d\dots 1})$ are suppressed by multiplying $\langle \hat{O} \rangle_{(\Delta_1^{\text{AD}} \rho_{d\dots 1})^{\text{real}}}$ by τ (the second term in the right-hand side of the first line of Eq. (8)). This is because the lowest-order error AD effect on the implementation of $\Delta_1^{\text{AD}} \rho_{d\dots 1}$, which is $\delta_1^{\text{AD}}(\Delta_1^{\text{AD}} \rho_{d\dots 1})$, becomes $\mathcal{O}(\tau^2)$ due to the multiplication by τ : $\delta^{\text{AD}}(\Delta_1^{\text{AD}} \rho_{d\dots 1}) \rightarrow \tau \cdot \delta^{\text{AD}}(\Delta_1^{\text{AD}} \rho_{d\dots 1}) = \sum_{p=1}^{\infty} \tau^{p+1} \cdot \delta_p^{\text{AD}}(\Delta_1^{\text{AD}} \rho_{d\dots 1})$. Consequently, in the first-order perturbation theory with respect to τ we have established our QEM scheme by the usage of the AD-effect circuit group and is expressed by the formula given by Eq. (8). The above argument on QEM-scheme derivation can be straightforwardly generalized to register-bit systems for $N_q \geq 2$. In this case, $\tilde{\rho}_{k\dots 1}^{\text{AD}}$ in Eq. (3) is represented as

$$\begin{aligned} \tilde{\rho}_{k\dots 1}^{\text{AD}} &= \mathcal{L}_{\text{AD}}[\rho_{k\dots 1}] \\ &= \sum_{j=0}^{N_q-1} -\frac{\rho_{k\dots 1}}{4} + \frac{Z_j \rho_{k\dots 1} Z_j}{4} + \tilde{\sigma}_j^- \rho_{k\dots 1} \tilde{\sigma}_j^+ \\ &\quad - P_j^1 \rho_{k\dots 1} P_j^1. \end{aligned} \quad (9)$$

We can apply our QEM scheme to the N_q register-bit system in the following way. We prepare N_q register bits and one ancilla bit $\{Q_{r0}, Q_{r1}, \dots, Q_{rN_q-1}, Q_a\}$. Then we create an ensemble of quantum circuits composed of the j -th register bit Q_{rj} ($j = 0, 1, \dots, N_q - 1$) and the ancilla bit Q_a which describes that Q_{rj} is subject to the AD effect induced by the ancilla bit Q_a . Namely, we create the ensemble of four types of quantum circuits composed of Q_{rj} and Q_a , the original quantum circuits given by U^{QC} , the quantum circuits with additional Z -gate operations, and the AD-effect circuits A and B. By summing up all these quantum circuits, we obtain the AD-effect circuit group which enables us to perform QEM for N_q -register-bit system under the AD effect. The total number of quantum circuits which compose the AD-effect

circuit group is $3dN_q + 1$, and thus, it scales polynomial in dN_q , which is not so high-cost computational performance.

Several comments are given in order. Firstly, we can extend our QEM formalism into cases of other quantum noises including generalized amplitude damping (GAD), phase damping (PD), their composite channels, and stochastic Pauli noise models such as bit flip, phase flip, bit-phase flip, and depolarizing channel. Secondly, we can create quantum-noise-effect circuit groups which enable us to perform QEM for higher-order quantum noise effects. We present the arguments on these two cases in Appendix A. Thirdly, we have set the gate time Δt to be equivalent for all the gates. For real quantum devices, however, the gate times are not equivalent, for instance, the gate times for the single-qubit gates are shorter than those of the two-qubit gates. Despite this situation, we can extend our QEM formalism for cases of gate times not being equivalent since the orders of the gate times are approximately the same as we discuss in subSec. III D. In addition, in the above analysis we have considered the situation where the quantum noise strength is homogeneous for all qubits. In real situations, however, quantum noise strengths might be inhomogeneous due to imperfect fabrication of quantum devices. Nevertheless, we can similarly and easily extend our QEM scheme to such cases since the quantum noise strengths are considered to be in the same order. Finally, we stress the fea-

ture of our proposed method by comparing with two other representative QEM methods using the following quantities, the number of register qubits N_q , the depth of quantum algorithm to be ran, the number of ancillary qubits N_a , and the number of additional quantum circuits N_{AQC} . In Table I, we summarize and present the comparison between our QEM method and the others. Here k is the order of the perturbation theory of our QEM method. First, let us make a comparison with zero noise extrapolation (ZNE) [48, 50]. This method does not require ancilla bits but requires additional quantum circuits for various noise strengths, from which ideal values are estimated. We write the number of noise strengths to perform ZNE by N_τ and denote them by $\gamma_0, \gamma_1, \dots < \gamma_{N_\tau-1}$: for ZNE $N_{\text{AQC}} = N_\tau$. In practice, N_τ is not relatively a large number and ZNE can be conducted without depending on N_q

TABLE I. Comparison of the QEM methods

Method	N_a	N_{AQC}
ZNE [48, 50]	0	N_τ
PEC [48, 51]	0	$\mathcal{O}(e^{2b\epsilon d})$
Our proposed method	k	$\mathcal{O}(\{dN_q\}^k)$

and d which means that QEM cost is relatively small but its quality gets worse provided that γ_0 is small enough. Our QEM method, on the other hand, requires ancilla qubits and the value of N_{AQC} for doing k -th order perturbation calculation is $\mathcal{O}(\{dN_q\}^k)$, which is in general higher than N_τ . Nevertheless, in principle our QEM method can be applied for any value of noise strength γ by doing higher-order perturbation calculation and the quality of our method becomes higher for larger k . Second, let us make a comparison with probabilistic error cancellation (PEC) [48, 51]. Like ZNE, PEC can recover zero-noise values without any ancillary qubit while it is necessary to prepare additional quantum circuits and the number of them scales exponentially with respect to the product of error rate of gates ϵ and d , i.e., $N_{\text{AQC}} \sim \mathcal{O}(e^{2b\epsilon d})$, where b is real positive value [26]. As discussed previously, in our QEM method although we need ancilla bits we can do higher-order perturbation calculation such that $N_{\text{AQC}} \sim \mathcal{O}(\{dN_q\}^k)$, which is polynomial in dN_q and is lower than N_{AQC} for PEC.

III. NUMERICAL SIMULATIONS

In this section, we numerically demonstrate our QEM scheme for four types of algorithms. For the quantum noise effect we choose AD effect. In subSec. III A, as a preliminary of our QEM demonstration, we present the results of two algorithms: the algorithm composed of the initial X -gate operation and the repetition of the Hadamard gate acting on a single register bit and that composed of the initial $X \otimes X$ operation and the controlled-Hadamard gate acting on two register bits. In subSec. III B, we show the results of QEM for a long-term quantum algorithm and here we choose quantum amplitude amplification (QAA) algorithm (Grover's search algorithm). In subSec. III C, we show the results of recently developed NISQ quantum algorithms, Quantum Approximate Optimization Algorithm (QAOA). In subSec. III D, we discuss the validity of our QEM scheme under the conditions of NISQ-device parameters.

In the following, let us explain the formalism of our noisy quantum simulations (numerical simulations of running quantum algorithms with real quantum devices performed by classical computers). As shown in Fig. 2, every time we apply an unitary (gate) operation, the N_q register bits experience AD effects. Suppose that at a time t_0 the quantum states of the register bits were given by the density matrix $\rho(t_0)$. According to the quantum master equation (1), when the unitary gate U has been applied to the register bits within the time interval Δt the quantum state of the register bits at $t = t_0 + \Delta t$ is expressed by the density matrix

$$\rho^{\text{AD}}(t_0 + \Delta t) = \mathcal{E}^{\text{AD}}[U\rho(t_0)U^\dagger], \quad (10)$$

where $\mathcal{E}^{\text{AD}}[\dots]$ is the superoperator which describes the AD effect on the N_q register bits and it is given by

$$\begin{aligned}\mathcal{E}^{\text{AD}}[\rho] &= \sum_{n_{Q_{r0}}, \dots, n_{Q_{rN_q-1}}} \mathcal{M}_{n_{Q_{r0}}, \dots, n_{Q_{rN_q-1}}} \cdot \rho \cdot \mathcal{M}_{n_{Q_{r0}}, \dots, n_{Q_{rN_q-1}}}^\dagger, \\ \mathcal{M}_{n_{Q_{r0}}, \dots, n_{Q_{rN_q-1}}} &= \mathcal{M}_{n_{Q_{r0}}}^{\text{AD}} \otimes \dots \otimes \mathcal{M}_{n_{Q_{rN_q-1}}}^{\text{AD}}, \\ \mathcal{M}_0^{\text{AD}} &= \begin{bmatrix} 0 & \sin\left(\frac{\vartheta_\tau}{2}\right) \\ & 0 \end{bmatrix}, \quad \mathcal{M}_1^{\text{AD}} = \begin{bmatrix} 1 & 0 \\ 0 & \cos\left(\frac{\vartheta_\tau}{2}\right) \end{bmatrix},\end{aligned}\tag{11}$$

where $n_{Q_{r0}}, \dots, n_{Q_{rN_q-1}} = 0, 1$, and $\cos^2\left(\frac{\vartheta_\tau}{2}\right) = e^{-\tau}$. The operators $\mathcal{M}_0^{\text{AD}}$ and $\mathcal{M}_1^{\text{AD}}$ are the Kraus operators acting on single-qubit states and describe the influence of the AD effect on a single register bit during the time interval Δt . Here we assume that the N_q register bits homogeneously experience the single-qubit-state AD effect as described in Eq. (11).

For later convenience, let us introduce the notation which describes the operation of the unitary operator U on the quantum state ρ by $\mathcal{T}[\rho, U](= U\rho U^\dagger)$. Let us write the quantum state generated by the unitary transformation U^{QC} under the AD effect by $\rho_{d\dots 1}^{\text{AD}}$. By using the superoperator $\mathcal{E}^{\text{AD}}[\dots]$, the output state $\rho_{d\dots 1}^{\text{AD}}$ is represented as

$$\rho_{d\dots 1}^{\text{AD}} = \mathcal{E}^{\text{AD}}[\mathcal{T}[\dots \mathcal{E}^{\text{AD}}[\mathcal{T}[\mathcal{E}^{\text{AD}}[\mathcal{T}[\rho(0), U_1], U_2], \dots U_d]]].\tag{12}$$

Eqs. (11) and (12) are the basic equations of our noisy quantum simulations. Namely, we perform our noisy quantum simulations by identifying the quantum state $\rho_{d\dots 1}^{\text{AD}}$ in the above equation with $\rho_{d\dots 1}^{\text{real}}$, which is the AD-affected quantum state generated by the unitary transformation U^{QC} on real devices. We conduct QEM described by Eq. (8) for various values of τ by tuning the value of ϑ_τ .

For performing our noisy quantum simulations, we have created two types of numerical codes. The first one is our original numerical code and the second one is the numerical code created by Qiskit [76]. The difference between these two codes is that the latter is programmed by the two numbers, N_{QC} and N_{samp} . The number N_{QC} describes the repetition number of quantum computation owing to the given quantum circuit whereas the number N_{samp} describes how many times you conduct the sampling for the expectation values of physical operators obtained by the N_{QC} -repeated quantum computation. Owing to this sampling, the repetitive number of the quantum computations effectively becomes $N_{\text{QC}} \times N_{\text{samp}}$, and our simulation results become more trustable. In our simulations we take $N_{\text{QC}} = 2^{10}$ and $N_{\text{samp}} = 100$. Our original numerical code, on the other hand, is the code for a noisy quantum simulation in the limit $N_{\text{QC}} \rightarrow \infty$, and basically, it performs pure linear algebraical computations such as matrix-product and trace operations. We note that when we create the numerical codes with Qiskit, we need to be careful with how controlled-unitary operators are implemented. On Qiskit program, the controlled-unitary operators are implemented as the decomposition of U_{CX} gates and single-qubit unitary gates. For example, the control- R_y gate $U_{CR_y(\vartheta)}[Q_{r1}; Q_{r0}]$ is decomposed as $U_{CR_y(\vartheta)}[Q_{r1}; Q_{r0}] = \left(\mathbf{1}_{2 \times 2 Q_{r0}} \otimes R_y(-\vartheta/2)_{Q_{r1}}\right) \cdot$

$U_{CX}[Q_{r1}; Q_{r0}] \cdot \left(\mathbf{1}_{2 \times 2 Q_{r0}} \otimes R_y(\vartheta/2)_{Q_{r1}}\right) \cdot U_{CX}[Q_{r1}; Q_{r0}]$. Therefore, when we simulate QAA for three-qubit systems and QAOA with our original code we implement $U_{CR_y(\vartheta)}[Q_{r1}; Q_{r0}]$ in the same way as Qiskit program does.

In order to quantitatively describe the validity of our QEM scheme we introduce the measure defined by

$$\text{RT}_{\text{QEM}} = \frac{|\langle \hat{O} \rangle_{\rho_{d\dots 1}^{\text{real}}} - \langle \hat{O} \rangle_{\rho_{d\dots 1}}|}{|\langle \hat{O} \rangle_{\rho_{d\dots 1}} - \langle \hat{O} \rangle_{\rho_{d\dots 1}^{\text{QEM}}}|}.\tag{13}$$

The numerator of RT_{QEM} in Eq. (13) describes the absolute of the difference between the expectation value owing to the noisy quantum simulation ($\langle \hat{O} \rangle_{\rho_{d\dots 1}^{\text{real}}}$) and the ideal expectation value ($\langle \hat{O} \rangle_{\rho_{d\dots 1}^{\text{ideal}}}$). On the other hand, the denominator represents the absolute of the difference between the expectation value obtained by our QEM scheme ($\langle \hat{O} \rangle_{\rho_{d\dots 1}^{\text{QEM}}}$, see Eq. (8) and the ideal expectation value. In other words, the measure RT_{QEM} in Eq. (13) is the ratio between the absolute of the error without QEM and the one with QEM. Thus, when $\text{RT}_{\text{QEM}} > 1$ the expectation value $\langle \hat{O} \rangle_{\rho_{d\dots 1}^{\text{QEM}}}$ is closer to the ideal value than $\langle \hat{O} \rangle_{\rho_{d\dots 1}^{\text{real}}}$, which means that our QEM scheme is working. In addition to the ratio RT_{QEM} in Eq. (13), we display the results of ideal simulations, noisy simulations, and noisy simulations with QEM, and show explicitly the validity of our QEM scheme. Note that for our original code we take the noise-strength parameter to be $\vartheta_\tau = i_0 \times 0.01$ with $i_0 = 0, 1, \dots, 50$ while for Qiskit code we take $\vartheta_\tau = i_Q \times 0.05$ with $i_Q = 0, 1, \dots, 10$. For computing the expectation values we include the cases $i_0 = 0$ and $i_Q = 0$ whereas for computing the ratio RT_{QEM} we omit $i_0 = 0$ and $i_Q = 0$. This is because in these two cases we have $\langle \hat{O} \rangle_{\rho_{d\dots 1}} = \langle \hat{O} \rangle_{\rho_{d\dots 1}^{\text{real}}} = \langle \hat{O} \rangle_{\rho_{d\dots 1}^{\text{QEM}}}$

and we encounter in the indefinite $\frac{0}{0}$. In the following, we create a subsection for each quantum algorithm and discuss the results in detail.

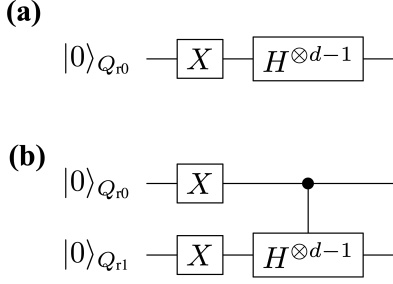


FIG. 5. Quantum circuits for (a) $U_{\text{pre1}}^{\text{QC}} = H^{\otimes d-1} \cdot X$ and (b) $U_{\text{pre2}}^{\text{QC}} = (U_{CH}[Q_{r0}; Q_{r1}])^{\otimes d-1} \cdot X_{Q_{r0}} \otimes X_{Q_{r1}}$.

A. Preliminary

As a preliminary, let us conduct the noisy quantum simulations for two simple algorithms. The first algorithm is given by the unitary operation $U_{\text{pre1}}^{\text{QC}} = H^{\otimes d-1} \cdot X$, where H denotes the Hadamard gate. The second one is given by $U_{\text{pre2}}^{\text{QC}} = (U_{CH}[Q_{r0}; Q_{r1}])^{\otimes d-1} \cdot X_{Q_{r0}} \otimes X_{Q_{r1}}$. The unitary operator $U_{CH}[Q_{r0}; Q_{r1}]$ is the controlled-Hadamard gate composed of the control bit Q_{r0} and the target bit Q_{r1} . Here we take the circuit depth d to be $d = 1 + 2^n$ with n being positive integers. Let us show the quantum circuits for these two algorithms in Fig. 5. By changing the values of d and τ , we numerically analyze how well our QEM scheme works in terms of these two parameters. Let us discuss from the results of noisy quantum simulations conducted by the quantum circuit in Fig. 5 (a) and show them in Fig. 6. We have taken the physical operators \hat{O} as $\hat{O} = X, Z$. The horizontal axis represents ϑ_τ , which can be regarded as the strength of AD effect. On the other hand, the vertical axis in Figs. 6(a,b) denote the expectation values of \hat{O} while those in Figs. 6(c,d) describe the ratio RT_{QEM} given in Eq. (13): Figs. 6(a,c) are the results for $\hat{O} = X$ while Figs. 6(b,d) are those for $\hat{O} = Z$. The dotted lines in Figs. 6(a,b) describe the expectation values without QEM being performed whereas the solid lines represent the expectation values with QEM being performed. For both the dotted and solid lines the red, blue, and green plots in Figs. 6 (a) and (b) are the computational results of $\langle X \rangle$ and $\langle Z \rangle$ for $d = 2^3 + 1, 2^4 + 1$, and $2^5 + 1$, respectively. The black dotted lines are the results of the ideal simulations. Let us analyze our simulation results by comparing the behaviors of the expectation values and the ratio RT_{QEM} in Eq. (13) as functions of ϑ_τ . In this way, we can clearly see whether our QEM scheme is working or not, and for this purpose in the following we rewrite $\langle \hat{O} \rangle_{\rho_{d \dots 1}}$, $\langle \hat{O} \rangle_{\rho_{d \dots 1}^{\text{real}}}$, $\langle \hat{O} \rangle_{\rho_{d \dots 1}^{\text{QEM}}}$, and RT_{QEM} as $\langle \hat{O} \rangle_{\rho_{d \dots 1}}(\vartheta_\tau)$, $\langle \hat{O} \rangle_{\rho_{d \dots 1}^{\text{real}}}(\vartheta_\tau)$, $\langle \hat{O} \rangle_{\rho_{d \dots 1}^{\text{QEM}}}(\vartheta_\tau)$, and $\text{RT}_{\text{QEM}}(\vartheta_\tau)$, respectively, to emphasize that they are the functions of ϑ_τ . Furthermore, we introduce the angle ϑ_τ^c such

that $\text{RT}_{\text{QEM}}(\vartheta_\tau = \vartheta_\tau^c) = 1$, which indicates that the point $\vartheta_\tau = \vartheta_\tau^c$ is the critical point of our QEM to become failed. Let us look from the results shown in Figs. 6(a,c) by focusing on how the behaviors of $\langle \hat{O} \rangle_{\rho_{d \dots 1}}$, $\langle \hat{O} \rangle_{\rho_{d \dots 1}^{\text{real}}}$, $\langle \hat{O} \rangle_{\rho_{d \dots 1}^{\text{QEM}}}$, and RT_{QEM} change by increasing ϑ_τ . In Fig. 6(a), as the definition of ϑ_τ^c we certainly see that in the range $0 < \vartheta_\tau \leq \vartheta_\tau^c$ the absolute $|\langle \hat{O} \rangle_{\rho_{d \dots 1}^{\text{real}}} - \langle \hat{O} \rangle_{\rho_{d \dots 1}}|$ is bigger than $|\langle \hat{O} \rangle_{\rho_{d \dots 1}^{\text{QEM}}} - \langle \hat{O} \rangle_{\rho_{d \dots 1}}|$, which implies that $\langle \hat{O} \rangle_{\rho_{d \dots 1}^{\text{QEM}}}$ is numerically closer to $\langle \hat{O} \rangle_{\rho_{d \dots 1}}$ than $\langle \hat{O} \rangle_{\rho_{d \dots 1}^{\text{real}}}$, and correspondingly, in Fig. 6(c) we see $\text{RT}_{\text{QEM}}(\vartheta_\tau) \geq 1$. As we increase the value of ϑ_τ from ϑ_τ^c , the absolute $|\langle \hat{O} \rangle_{\rho_{d \dots 1}^{\text{real}}} - \langle \hat{O} \rangle_{\rho_{d \dots 1}}|$ becomes smaller than $|\langle \hat{O} \rangle_{\rho_{d \dots 1}^{\text{QEM}}} - \langle \hat{O} \rangle_{\rho_{d \dots 1}}|$, and correspondingly, the ratio $\text{RT}_{\text{QEM}}(\vartheta_\tau)$ decreases monotonically from one. For the region $\vartheta_\tau \geq \vartheta_\tau^c$ to improve the quality of our QEM we need take into account higher-order AD effects and establish QEM schemes for mitigating them and we expect the value of ϑ_τ^c to become larger. Next, let us analyze how the quality of our QEM becomes when we vary the circuit depth d . We see that for every ϑ_τ both $|\langle \hat{O} \rangle_{\rho_{d \dots 1}^{\text{real}}} - \langle \hat{O} \rangle_{\rho_{d \dots 1}}|$ and $|\langle \hat{O} \rangle_{\rho_{d \dots 1}^{\text{QEM}}} - \langle \hat{O} \rangle_{\rho_{d \dots 1}}|$ become bigger and $\text{RT}_{\text{QEM}}(\vartheta_\tau)$ decreases as we increase d . This is reasonable because when d gets larger the amount of error gets bigger. For the results in Figs. 6(b,d), basically we see that both the expectation values of Z and $\text{RT}_{\text{QEM}}(\vartheta_\tau)$ show the similar behaviors as those for $\hat{O} = X$: (I) the validity of QEM ($\text{RT}_{\text{QEM}}(\vartheta_\tau) \geq 1$) in the range $0 < \vartheta_\tau \leq \vartheta_\tau^c$ and monotonic decrease of $\text{RT}_{\text{QEM}}(\vartheta_\tau)$ for $\vartheta_\tau > \vartheta_\tau^c$, and (II) worsening of the quality of our QEM for large d . In contrast to the above characteristics of $\langle X \rangle$ and $\langle Z \rangle$, we have numerically verified that the expectation value of Y takes zero for any ϑ_τ . This is because when the density matrix ρ is a real matrix the expectation value $\langle Y \rangle$ is zero. Since both the quantum algorithm and the AD effect are described by real numbers (see also Eq. (7) or the Kraus operators in Eq. (11) the density matrix generated by these two things is real and we have $\langle Y \rangle = 0$.

Let us discuss the results in Fig. 7. They are the noisy simulation results of the quantum algorithm given by $U_{\text{pre2}}^{\text{QC}}$ (see the quantum circuit in Fig. 5) and we have taken $d = 1 + 2^n$ as in the case of simulations for $U_{\text{pre1}}^{\text{QC}}$. Here we have simulated $\text{RT}_{\text{QEM}}(\vartheta_\tau)$ for the expectation values of the operators $\hat{O} = ZX, ZZ$. Overall, we see the same characteristics with the cases of $\hat{O} = X, Z$: the characteristics (I) and (II) mentioned above. For any ϑ_τ , the ratio $\text{RT}_{\text{QEM}}(\vartheta_\tau)$ for the noisy simulations of $U_{\text{pre2}}^{\text{QC}}$ are smaller than those of $U_{\text{pre1}}^{\text{QC}}$. This is because $U_{\text{pre1}}^{\text{QC}}$ is solely comprised of the single-qubit gates (X and H) while $U_{\text{pre2}}^{\text{QC}}$ is constructed by n -operation of the controlled-Hadamard gate (two-qubit gate), and thus, the bigger amount of errors are accumulated in the latter case. The difference between the characteristics of noisy simulations for $U_{\text{pre1}}^{\text{QC}}$ and those for $U_{\text{pre2}}^{\text{QC}}$, although it is not an essential point for the validity of our QEM, is that we see one minima and one maxima in the plots for $\text{RT}_{\text{QEM}}(\vartheta_\tau)$ (Figs. 7(c,d)). Let us denote the point where $\text{RT}_{\text{QEM}}(\vartheta_\tau)$ takes the minimum (maximum) by $\vartheta_\tau^{\text{min}}$ ($\vartheta_\tau^{\text{max}}$): note that these values depend on d . We can understand why these points emerge by

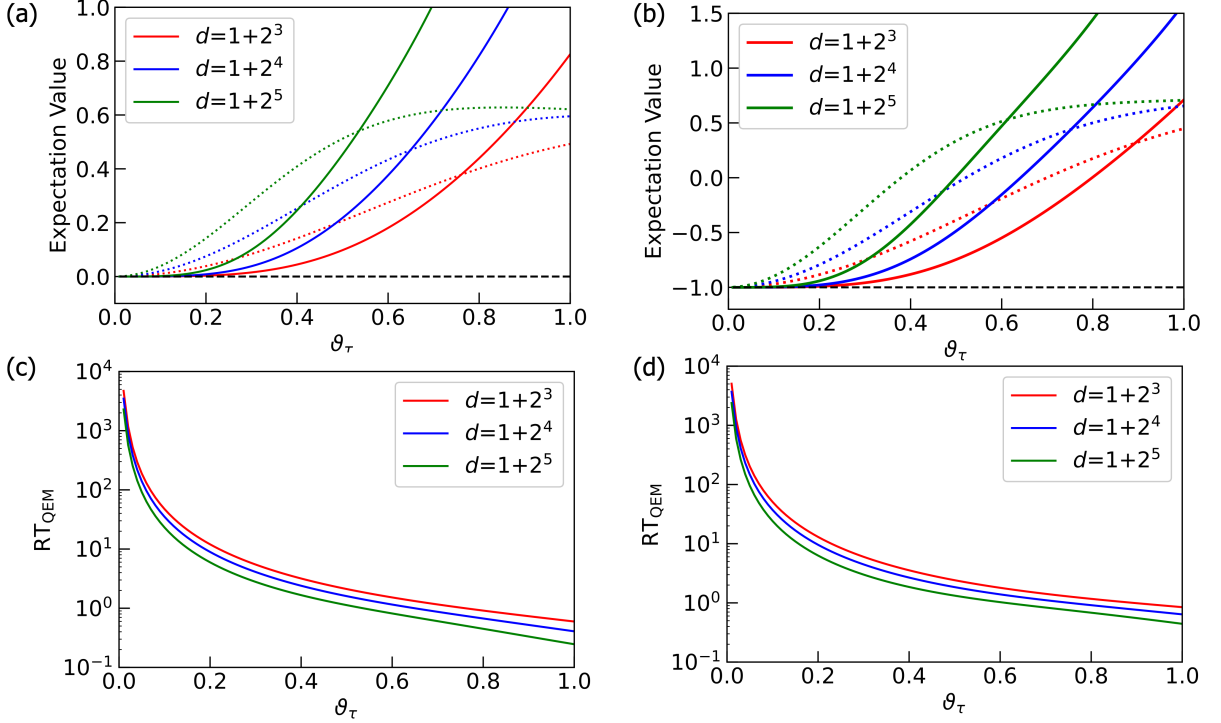


FIG. 6. Quantum simulations for the quantum algorithm $U_{\text{pre1}}^{\text{QC}} = H^{\otimes d-1} \cdot X$. Plots in (a) and (b) are the results of QEM for the expectation value of X and Z , respectively. The dotted lines are the expectation values without QEM while the solid lines represent the expectation values with QEM. The black dotted lines are the results of the ideal simulations. In (c) and (d), we show the ratio RT_{QEM} for the expectation values of X and Z respectively. The red, blue, and green plots are the results for $d = 1 + 2^3$, $d = 1 + 2^4$, and $d = 1 + 2^5$, respectively.

looking at Figs. 7(a,b). In the range $0 < \vartheta_\tau \leq \vartheta_\tau^{\min}$ we have $\langle \hat{O} \rangle_{\rho_{d \dots 1}^{\text{real}}} < \langle \hat{O} \rangle_{\rho_{d \dots 1}^{\text{QEM}}}$ whereas in the range $\vartheta_\tau^{\min} < \vartheta_\tau \leq \vartheta_\tau^{\max}$ we have $\langle \hat{O} \rangle_{\rho_{d \dots 1}^{\text{real}}} > \langle \hat{O} \rangle_{\rho_{d \dots 1}^{\text{QEM}}}$. Then, in the range $\vartheta_\tau^{\max} < \vartheta_\tau$ we have $\langle \hat{O} \rangle_{\rho_{d \dots 1}^{\text{real}}} < \langle \hat{O} \rangle_{\rho_{d \dots 1}^{\text{QEM}}}$. As a result, the minima appears at $\vartheta_\tau = \vartheta_\tau^{\min}$ whereas the maxima emerges at $\vartheta_\tau = \vartheta_\tau^{\max}$. Likewise the case of the noisy simulations of $U_{\text{pre1}}^{\text{QC}}$, the density matrices are generated as real matrices (the unitary transformation $U_{\text{pre2}}^{\text{QC}}$ as well as the AD effects are described by real numbers), and the expectation values of the Pauli operators, IY, XY, YI, YX, YZ, ZY are zero for both ideal and noisy simulations. Here we have rewritten $\mathbf{1}_{2 \times 2}$ as I for convenience. Note that the expectation value of the identity operator ($= \mathbf{1}_{4 \times 4}$: four by four identity operator) is one for any quantum state including noise-affected quantum states since the trace of density matrix is one for any quantum state. In other words, it is unnecessary to do QEM for the expectation value of the identity operator.

B. Quantum Amplitude Amplification

By taking account of the previous analysis, let us apply our QEM scheme to Quantum Amplitude Amplification (QAA) [32] for three-qubit systems: two-register bits and one oracle bit. One of the important application of QAA is the database retrieval and the quantum algorithms for this is called the Grover's search algorithm [32, 77–80]. Let us denote the (classical) oracle function by f and a binary by x which takes “00”, “01”, “10”, “11”. We consider that we have only one solution of f and write it by x^* , which satisfy $f(x^*) = 1$, and assume $x^* = “11”$: for $x = “00”, “01”, “10”$ we have $f(x) = 0$. The oracle operator O_{QAA} can be implemented on a quantum circuit by using one oracle bit Q_o such that $O_{\text{QAA}} \left[|x\rangle_{Q_{r0}Q_{r1}} \otimes \left(\frac{|0\rangle_{Q_o} - |1\rangle_{Q_o}}{\sqrt{2}} \right) \right] = (-1)^{f(x)} \left[|x\rangle_{Q_{r0}Q_{r1}} \otimes \left(\frac{|0\rangle_{Q_o} - |1\rangle_{Q_o}}{\sqrt{2}} \right) \right]$, where the superposition state $\frac{|0\rangle_{Q_o} - |1\rangle_{Q_o}}{\sqrt{2}}$ is created by applying $H \cdot X$ on the oracle-bit state $|0\rangle_{Q_o}$. In our case, $(-1)^{f(x)} = -1$ when $|x\rangle_{Q_{r0}Q_{r1}} = |11\rangle_{Q_{r0}Q_{r1}}$, and the oracle operator O_{QAA} is equivalent to the Toffoli gate comprised of the two controlled bits Q_{r0} and Q_{r1} and the target bit Q_o [32], and write it by $U_{\text{CX}}[Q_{r0}Q_{r1}; Q_o]$. To construct QAA we need one more unitary transformation and that is $U_\psi = (\mathbf{1}_{4 \times 4} - 2|\psi\rangle\langle\psi|) \otimes \mathbf{1}_{2 \times 2}$, where $|\psi\rangle = H^{\otimes 2}|00\rangle_{Q_{r0}Q_{r1}}$. By introducing $U_{\text{init}} = H^{\otimes 2} \otimes (H \cdot X)_{Q_o}$, QAA is given by the unitary operation [32]

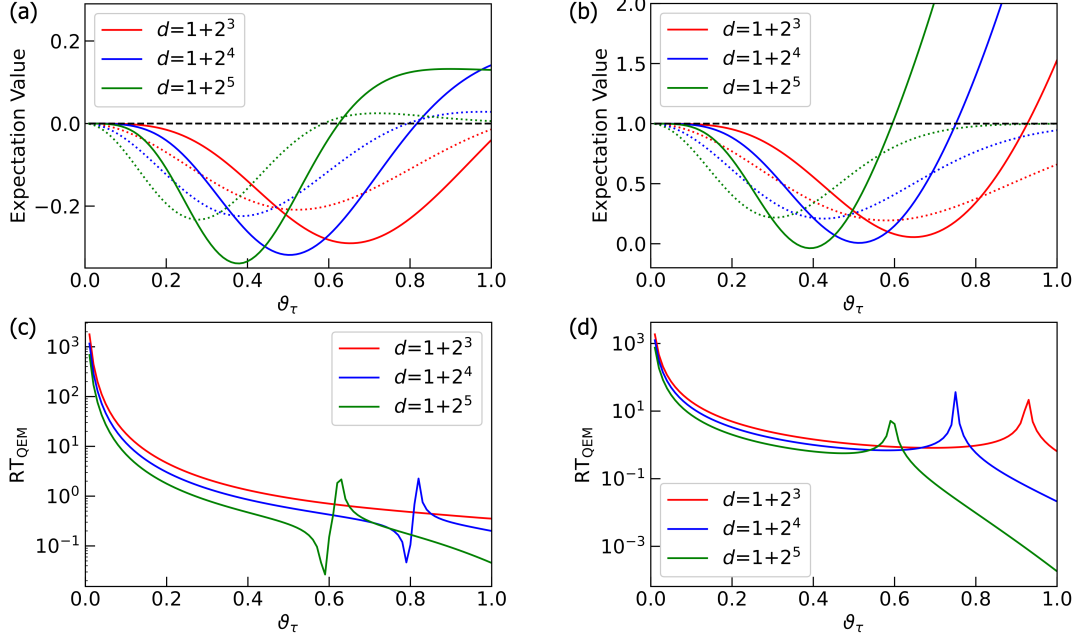


FIG. 7. Quantum simulations for the quantum algorithm $U_{\text{pre2}}^{\text{QC}} = (U_{\text{CH}}[Q_{r0}; Q_{r1}]^{\otimes d-1}) \cdot X_{Q_{r0}} \otimes X_{Q_{r1}}$. Plots in (a) and (b) are the results of QEM for the expectation value of ZX and ZZ , respectively. The dotted lines are the expectation values without QEM while the solid lines represent the expectation values with QEM. The black dotted lines are the ideal simulation results. We plot the ratio RT_{QEM} for expectation value of ZX and ZZ in (c) and (d), respectively. The red, blue, and green plots are the results for $d = 1 + 2^3$, $d = 1 + 2^4$, and $d = 1 + 2^5$, respectively.

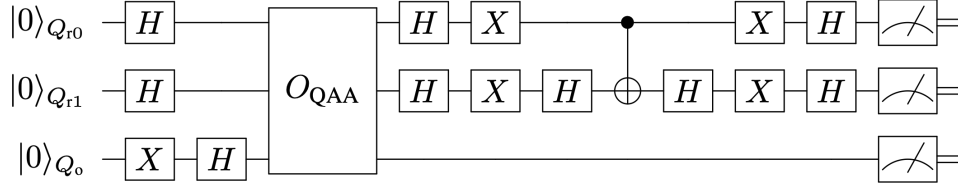


FIG. 8. Quantum circuits for U^{QAA} in Eq. (14).

$$\begin{aligned}
 U^{\text{QAA}} &= (U_{\text{G}})^k \cdot U_{\text{init}}, \\
 U^{\text{G}} &= -U_{\psi} \cdot O_{\text{QAA}}, \\
 U_{\psi} &= ((X \cdot H)^{\otimes 2} \otimes \mathbf{1}_{2 \times 2, Q_o}) \cdot (\mathbf{1}_{2 \times 2, Q_{r0}} \otimes H_{Q_{r1}} \otimes \mathbf{1}_{2 \times 2, Q_o}) \cdot (U_{\text{CX}}[Q_{r0}; Q_{r1}] \otimes \mathbf{1}_{2 \times 2, Q_o}) \\
 &\quad \cdot (\mathbf{1}_{2 \times 2, Q_{r0}} \otimes H_{Q_{r1}} \otimes \mathbf{1}_{2 \times 2, Q_o}) \cdot ((X \cdot H)^{\otimes 2} \otimes \mathbf{1}_{2 \times 2, Q_o})
 \end{aligned} \tag{14}$$

We show the quantum circuit for the unitary operation U^{QAA} in Fig. 8 [32]: the quantum circuit for the oracle operator $O_{\text{QAA}} (= U_{\text{CX}}[Q_{r0}; Q_{r1}; Q_o])$ is shown in Appendix. B. We note that on the quantum circuit in Fig. 8, what is actually implemented is $-U^{\text{G}} = U_{\psi} \cdot O_{\text{QAA}}$ and the global phase factor (-1) does not affect our result. The unitary operation U_{G} is called the Grover operator and k is the repetitive number of its operation and here we have $k = 1$. After the operation of U^{QAA} in Eq. (14), ideally both of the probability weights of $|110\rangle$ and $|111\rangle$ are $\frac{1}{2}$, and thus, the probab-

ility of obtaining the quantum state $|11\rangle$ as the output state is $\frac{1}{2} \times 2 = 1$, which implies the success of searching the solution $x^* = "11"$. By taking account of the above theoretical framework, we examine whether our QEM scheme works or not for QAA given by U^{QAA} in Eq. (14) by computing the probability weights of $|110\rangle$ and $|111\rangle$ which we name as P_{110} and P_{111} , respectively, and show these results in Fig. 9. Solid lines in Figs. 9(a) and (b) describes the probability weights obtained by our original numerical code and we have denoted $\langle P_{110(111)} \rangle_{\rho_{d-1}^{\text{ideal}}}$, $\langle P_{110(111)} \rangle_{\rho_{d-1}^{\text{real}}}$, and $\langle P_{110(111)} \rangle_{\rho_{d-1}^{\text{QEM}}}$

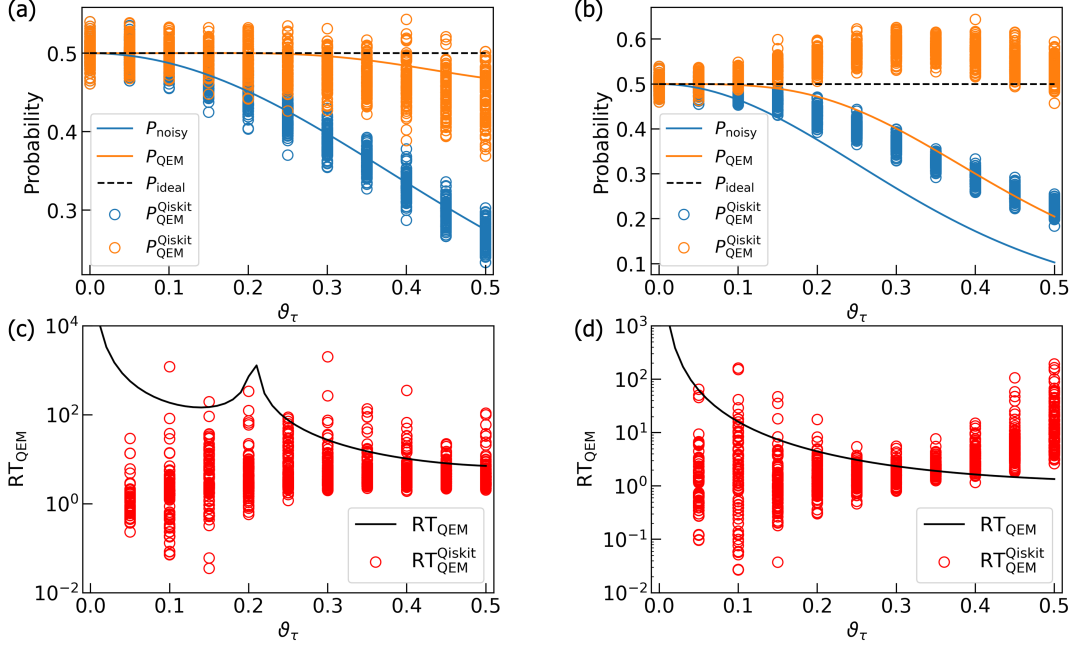


FIG. 9. Quantum simulation results for the quantum algorithm U^{QAA} in Eq. (14). Plots in (a) and (b) are the results of the probabilities P_{110} (probability of $|110\rangle$) and P_{111} (probability of $|111\rangle$), respectively. The dotted black lines are the ideal simulation results whereas the blue and orange curves are the noisy simulation results and the ones with QEM, respectively. All of them are obtained by our original code. The blue and orange circles are the noisy simulation results and the ones with QEM, respectively, and they are obtained by our Qiskit code. Plots in (c) and (d) are the results of the ratio RT_{QEM} for P_{110} and P_{111} , respectively. The black curves are obtained by our original code while the red circles by our Qiskit code. For each ϑ_τ we have plotted 100 circles in (a) - (d), i.e., $N_{\text{samp}} = 100$.

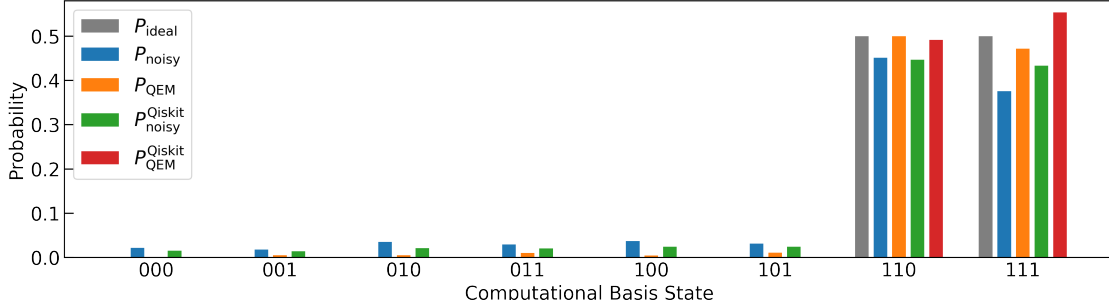


FIG. 10. Histogram of the probability distribution of the computational basis states for QAA simulations given by U^{QAA} in Eq. (14). Here we have set $\vartheta_\tau = 0.2$.

by P_{ideal} , P_{real} , and P_{QEM} , respectively. On the other hand, the blue and orange circles are calculated by our Qiskit code and we have denoted $\langle P_{110(111)} \rangle_{\rho_{d,\dots,1}^{\text{real}}}$ and $\langle P_{110(111)} \rangle_{\rho_{d,\dots,1}^{\text{QEM}}}$ by $P_{\text{noisy}}^{\text{Qiskit}}$ and $P_{\text{QEM}}^{\text{Qiskit}}$, respectively. Similarly, in Figs. 9(c) and (d), we have denoted the ratio RT_{QEM} calculated by our Qiskit code by RT_{QEM}^{Qiskit} . For the results obtained by our original code we have just used the notation RT_{QEM} for describing them. Let us look from the simulation results of P_{110} and the associated ratio RT_{QEM} given by Figs. 9(a) and (c), respectively. In the range $0 \leq \vartheta_\tau \leq 0.5$, overall the simulation results with QEM are numerically close to the ideal values than the noisy simulation results, and correspondingly, we have $RT_{QEM} > 1$.

The similar characteristics can be seen in Figs. 9(b) (simulation results of P_{111}) and (d) (RT_{QEM} for P_{111}). For the results obtained by our Qiskit code, the deviation between RT_{QEM} and RT_{QEM}^{Qiskit} becomes prominent in the small ϑ_τ region and we consider this as follows. When noise strength ϑ_τ is weak enough, on the Qiskit code the difference between the noisy value and the ideal value is very tiny such that our QEM becomes invalid and RT_{QEM}^{Qiskit} gets lower than one. On the other hand, we see that some red points are above $RT_{QEM} = 1$. We consider that by greatly increasing N_{QC} , we expect that RT_{QEM}^{Qiskit} approaches to RT_{QEM} . As a result, our QEM works for the noisy simulations of both P_{110} and P_{111} . Let us also show

the simulation results of the rest of the six probabilities of the computational basis states for $\vartheta_\tau = 0.2$ as the histogram in Fig. 10, which also includes P_{110} and P_{111} . The ideal values of these six probabilities are all zero and we see that the simulation results with QEM are numerically closer to them compared to the noisy simulation results, which indicates that our QEM scheme also works for the other six probabilities.

In addition to the above simulation, let us present the simplified version of QAA for the two-qubit systems [81]. In this problem setting, we consider the effective two-dimensional space spanned by the two Bell states $|\Psi^+\rangle = \frac{|01\rangle+|10\rangle}{\sqrt{2}}$ and $|\Phi^+\rangle = \frac{|00\rangle+|11\rangle}{\sqrt{2}}$, and write their superposition state by $|\Sigma\rangle = c_{\Psi^+}|\Psi^+\rangle + c_{\Phi^+}|\Phi^+\rangle$, where the complex coefficients c_{Ψ^+}, c_{Φ^+} satisfy $|c_{\Psi^+}|^2 + |c_{\Phi^+}|^2 = 1$. Our goal is to amplify the probability amplitude c_{Φ^+} . Here we take the initialization operator to be $V_{\text{init}} = UCX[Q_{r1}; Q_{r0}] \cdot (R_y(\frac{2\pi}{3})_{Q_{r0}} \otimes H_{Q_{r1}})$ while we take the Grover operator to be $V_G = (V_s V_\omega)^k$, where $V_\omega = (X \cdot Z \cdot X)_{Q_{r0}} \otimes Z_{Q_{r1}}$ and $V_s = V_{\text{init}} \cdot (2|0\rangle\langle 0| - \mathbf{1}_{4 \times 4}) \cdot V_{\text{init}}^\dagger \equiv -\tilde{V}_s$ with $\tilde{V}_s = V_{\text{init}} \cdot (X \otimes X \cdot UCZ[Q_{r0}; Q_{r1}] \cdot X \otimes X) \cdot V_{\text{init}}^\dagger [xxx]$. k is the number of V_G to be applied. In total, the unitary operation for running QAA is given by $V^{\text{QAA}} = (V_G)^k \cdot V_{\text{init}}$. We present the corresponding quantum circuit in Fig. 11. As similar to the above case, on the quantum circuit we implement \tilde{V}_s instead of V_s . In the following, let us take a look at the meanings of the three unitary operations V_{init}, V_s , and V_ω . First, the unitary operation V_{init} generates the superposition of $|\Phi^+\rangle$ and $|\Psi^+\rangle$ as $|00\rangle \rightarrow |s\rangle = V_{\text{init}}|00\rangle = \cos\frac{\theta_V}{2}|\Psi^+\rangle + \sin\frac{\theta_V}{2}|\Phi^+\rangle$ with $\theta_V = \pi/3$. Second, the unitary operation V_ω is the oracle operator and when it is applied to the initial state $|s\rangle$ we have $V_\omega|s\rangle = \cos\frac{\theta_V}{2}|\Psi^+\rangle - \sin\frac{\theta_V}{2}|\Phi^+\rangle$, i.e., the oracle operator V_ω is the operator such that it reverses the sign of the Bell state $|\Phi^+\rangle$. Third, $V_s = 2|s\rangle\langle s| - \mathbf{1}_{4 \times 4}$ is the reflection of the vector $V_\omega|s\rangle$ with respect to the vector $|s\rangle$. When we operate V_G on $|s\rangle$ for k times we have $(V_G)^k|s\rangle = \cos\frac{(2k+1)\theta_V}{2}|\Psi^+\rangle + \sin\frac{(2k+1)\theta_V}{2}|\Phi^+\rangle$, and since $\theta_V = \pi/3$ we have $k = 1$. We can understand the geometrical meaning of the operation V_G as follows. Let us consider the effective three-dimensional space spanned by the two Bell states $|\Phi^+\rangle$ and $|\Psi^+\rangle$ and the vector $|\xi\rangle$ which is perpendicular to both $|\Phi^+\rangle$ and $|\Psi^+\rangle$. Furthermore, we call the axis which is parallel to $|\xi\rangle$ (perpendicular to the two-dimensional plane spanned by $|\Phi^+\rangle$ and $|\Psi^+\rangle$) as ξ -axis. The unitary operation V_G is the rotation about ξ -axis by the angle 2ϑ in this effective three-dimensional space. We can verify whether $|\Phi^+\rangle$ has been generated as the output state or not by measuring the probabilities of $|00\rangle$ state and $|11\rangle$ state, which are denoted by p_{00} and p_{11} , respectively. In other words, the probabilities p_{00} and p_{11} are the expectation values of the projection operators P_{00} and P_{11} , respectively, where P_{00} (P_{11}) is the projection operator of $|00\rangle$ ($|11\rangle$) state. Namely, we run noisy quantum simulation for $\hat{O} = P_{00}, P_{11}$ and perform QEM on them: Note that in the case of the ideal simulation we obtain $p_{00} = p_{11} = \frac{1}{2}$. We plot the numerical results of p_{11} and p_{00} for the range $0 \leq \vartheta_\tau \leq 0.5$ in Figs. 12(a) and (b), respectively, and in Figs. 12(c) and (d) we plot $\text{RT}_{\text{QEM}}(\vartheta_\tau)$

for p_{11} and p_{00} , respectively. All these results shown here are obtained by our original numerical code and we have denoted $\langle P_{00(11)} \rangle_{\rho_{d \dots 1}^{\text{ideal}}}, \langle P_{00(11)} \rangle_{\rho_{d \dots 1}^{\text{real}}}$, and $\langle P_{00(11)} \rangle_{\rho_{d \dots 1}^{\text{QEM}}}$ by $P_{\text{ideal}}, P_{\text{real}}$, and P_{QEM} , respectively. Let us look from the results of the probability p_{11} . In Fig. 12(a) we see that for any ϑ_τ the absolute of the deviation $|\langle P_{11} \rangle_{\rho_{d \dots 1}^{\text{real}}} - \langle P_{11} \rangle_{\rho_{d \dots 1}}|$ is bigger than $|\langle P_{11} \rangle_{\rho_{d \dots 1}^{\text{QEM}}} - \langle P_{11} \rangle_{\rho_{d \dots 1}}|$, and correspondingly, as we see in Fig. 12(d) the ratio $\text{RT}_{\text{QEM}}(\vartheta_\tau)$ is greater than one. Therefore, our QEM scheme works well for the noisy simulation of p_{11} . In contrast, in Fig. 12(b) and (d) we see that the probability p_{00} shows essentially a different behavior. That is the expectation value without QEM $\langle P_{00} \rangle_{\rho_{d \dots 1}^{\text{real}}}$ is numerically closer to the ideal value $\langle P_{00} \rangle_{\rho_{d \dots 1}}$ ($= 0$) compared to the QEM-performed expectation value $\langle P_{00} \rangle_{\rho_{d \dots 1}^{\text{QEM}}}$, and correspondingly, the ratio $\text{RT}_{\text{QEM}}(\vartheta_\tau)$ is lower than one. Such a characteristic is understood as follows. Firstly, we have analytically examined that the expectation value $\langle P_{00} \rangle_{\rho_{d \dots 1}^{\text{real}}}$ does not include the first-order term in τ , i.e., $\langle P_{00} \rangle_{\Delta_1^{\text{AD}} \rho_{d \dots 1}} = 0$. The lowest-order term included in the numerator of $\text{RT}_{\text{QEM}}(\vartheta_\tau)$ is $\mathcal{O}(\tau^2)$. Secondly, due to our QEM the lowest order of the denominator of $\text{RT}_{\text{QEM}}(\vartheta_\tau)$ is also $\mathcal{O}(\tau^2)$. As a result, the ratio $\text{RT}_{\text{QEM}}(\vartheta_\tau)$ becomes lower than one, which indicates that it is not appropriate to adapt our QEM scheme. We consider that this is because our QEM scheme described by Eq. (8) is the scheme for mitigating the first-order AD effect. We note that in the limit of $\vartheta_\tau \rightarrow 0$, the ratio RT_{QEM} takes finite value, and analytically it is the ratio between the absolute of the coefficient of $\langle P_{00} \rangle_{\delta_2^{\text{AD}} \rho_{d \dots 1}}$ and that of $\langle P_{00} \rangle_{\delta_1(\Delta_1^{\text{AD}} \rho_{d \dots 1})}$. Moreover, when we use the Qiskit code the first-order term in τ appears for $\langle P_{00} \rangle_{\rho_{d \dots 1}^{\text{real}}}$ owing to the decomposition of $UCZ[Q_{r1}; Q_{r0}]$ gate given by $(\mathbf{1}_{2 \times 2 Q_{r0}} \otimes H_{Q_{r1}}) \cdot UCX[Q_{r1}; Q_{r0}] \cdot (\mathbf{1}_{2 \times 2 Q_{r0}} \otimes H_{Q_{r1}})$, and in such a case our QEM works well. Besides p_{00} and p_{11} , let us briefly discuss the noisy simulation results of the probability weights of $|01\rangle$ and $|10\rangle$ and write them by p_{01} and p_{10} , respectively. We show them in the histogram in Fig. 13 which describes the probability distribution of the computational basis states of the two register qubits Q_{r0} and Q_{r1} . Here we have taken $\vartheta_\tau = 0.2$. We see that like the probability weight of $|11\rangle$, our QEM scheme works for the probability weights of $|01\rangle$ and $|10\rangle$.

Let us end this subsection by giving the following comment. In the previous subsection, we have seen that our QEM scheme becomes meaningless in the cases where the expectation values of the ideal simulations are equivalent to those of noisy simulations such as the simulation for the expectation value $\langle Y \rangle$. Besides these cases, our QEM scheme represented by the formula in Eq. (8) does not work when noisy expectation values do not include the first-order term in τ like the noisy simulation for the probability p_{00} discussed above. In other words, if we construct the QEM formula which describes the mitigation for a higher-order quantum noise effect, which is discussed in Appendix A1, by using it we become able to accomplish the noisy quantum simulation obtaining $\text{RT}_{\text{QEM}} > 1$.

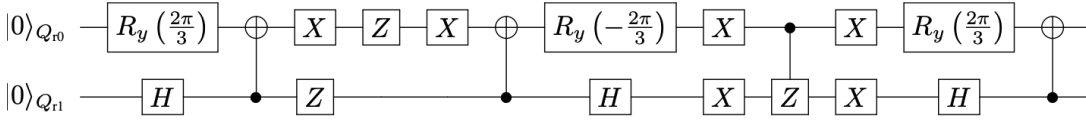


FIG. 11. Quantum circuit for QAA given by V^{QAA} with $k = 1$.

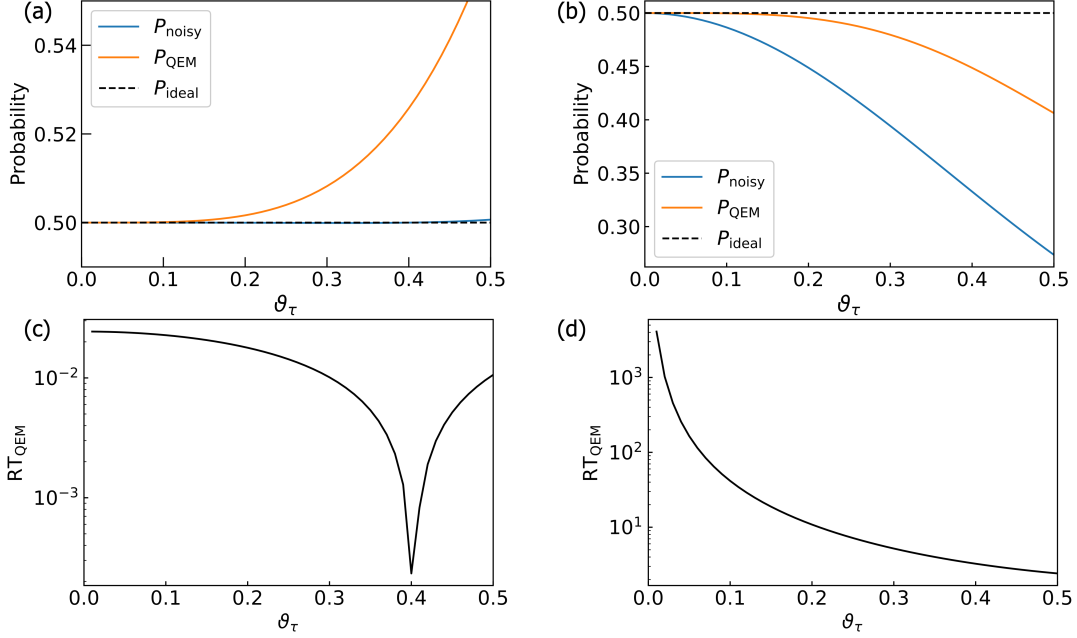


FIG. 12. Noisy quantum simulations for QAA given by V^{QAA} for $\hat{O} = P_{00}, P_{11}$. All these results are obtained by our numerical code. (a) Plots of the results of $P_{\text{ideal}} = \langle P_{00} \rangle_{\rho_{d \dots 1}}$, $P_{\text{noisy}} = \langle P_{00} \rangle_{\rho_{d \dots 1}^{\text{real}}}$, and $P_{\text{QEM}} = \langle P_{00} \rangle_{\rho_{d \dots 1}^{\text{QEM}}}$ presented by the black dashed line, the blue solid line, and the orange solid line, respectively. (b) Plots of the results of $P_{\text{ideal}} = \langle P_{11} \rangle_{\rho_{d \dots 1}}$, $P_{\text{noisy}} = \langle P_{11} \rangle_{\rho_{d \dots 1}^{\text{real}}}$, and $P_{\text{QEM}} = \langle P_{11} \rangle_{\rho_{d \dots 1}^{\text{QEM}}}$ presented by the black dashed line, the blue solid line, and the orange solid line, respectively. (c) The ratio $\text{RT}_{\text{QEM}}(\vartheta_\tau)$ for P_{00} . (d) The ratio $\text{RT}_{\text{QEM}}(\vartheta_\tau)$ for P_{11} .

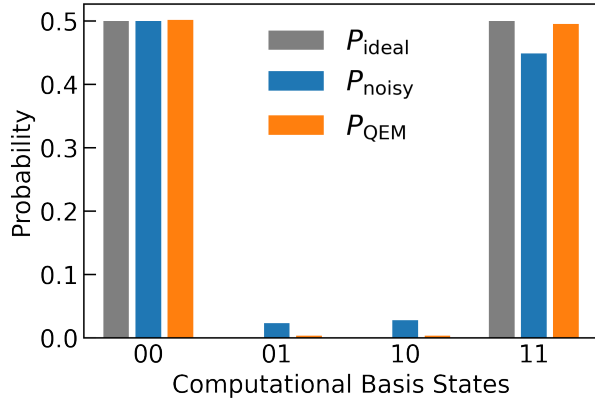


FIG. 13. Histogram of the probability distribution of the computational basis states for two-qubit-system QAA simulations. We have set $\vartheta_\tau = 0.2$.

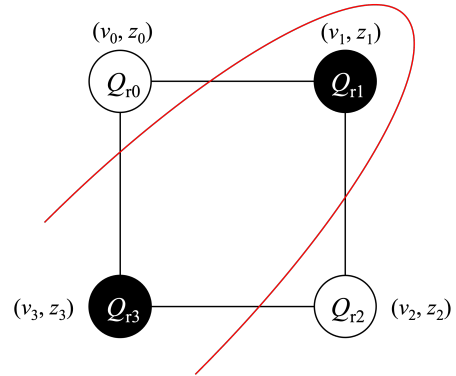


FIG. 14. Structure of the graph $G = (V, E)$. It is the square composed of the four vertices v_0, v_1, v_2 , and v_3 and the four edges $\langle v_0 v_1 \rangle, \langle v_1 v_2 \rangle, \langle v_2 v_3 \rangle$, and $\langle v_3 v_0 \rangle$. For each vertex v_i ($i = 0, 1, 2, 3$) the binary value $z_i = \pm 1$ is assigned and the set (v_i, z_i) is encoded in the qubit Q_{ri} in the QAOA simulation.

C. QAOA

As a final example, let us apply our QEM scheme to the noisy simulation of the variational quantum algorithm called Quantum Approximate Optimization Algorithm (QAOA) [26–32]. In the following, we analyze QAOA for a max-cut problem which is to divide vertices (nodes) of a given graph into two groups so that the number of edges connecting two vertices belonging to the different groups is maximized and is a NP (Non-deterministic Polynomial time)-hard problem.

First, we discuss from a theoretical framework of a classical approximate optimization. We express the given graph G as $G = (V, E)$, where $V = \{v_0, \dots, v_i, \dots, v_{N_V-1}\}$ is the set of vertices with N_V denoting their total number and for each vertex v_i the binary value $z_i = \pm 1$ is assigned. $E = \left\{ \{v_0 v_1\}, C_{0,1} \}, \dots, \{v_i v_{i+1}\}, C_{i,i+1} \}, \dots, \{v_{N_V-2} v_{N_V-1}\}, C_{N_V-2, N_V-1} \right\}$ is the set of the edges with $\langle v_i v_{i+1} \rangle$ denoting the edge connected by the vertices v_i and v_{i+1} . The quantity C_{ij} ($i, j = 0, \dots, N_V - 1$ with $i \neq j$) is the adjacency matrix element (weight) for the edge $\langle v_i v_j \rangle$ which is semi-positive. Let us write the N_V strings of z_i by $\mathbf{z} = (z_0, \dots, z_{N_V-1})$. The goal of a classical approximate optimization is to minimize the cost function

$$C(\mathbf{z}) = \frac{1}{2} \sum_{(v_i, v_j)} C_{ij} (z_i z_j - 1), \quad (15)$$

or equivalently to maximize the ratio $r_{\text{CAO}} (\leq 1)$ which satisfies

$$\frac{C(\mathbf{z})}{C_{\min}} \geq r_{\text{CAO}}, \quad (16)$$

where C_{\min} is the minimum value of $C(\mathbf{z})$. In our simulation, as illustrated in Fig. 14 we adopt the square graph given by the four vertices v_0, v_1, v_2 , and v_3 , and the edges are $\langle v_0 v_1 \rangle, \langle v_1 v_2 \rangle, \langle v_2 v_3 \rangle$, and $\langle v_3 v_0 \rangle$, and take $C_{ij} = 1$ for any edge $\langle v_i v_j \rangle$. Next, we discuss the theoretical framework for QAOA. The four vertices v_0, v_1, v_2 , and v_3 are encoded in four qubits Q_{r0}, Q_{r1}, Q_{r2} , and Q_{r3} , respectively, and the values $z_i z_j$ in the expectation values of the operators $Z_{Q_{ri}} \otimes Z_{Q_{rj}}$. The cost function $C(\mathbf{z})$ in Eq. (15) is given by the expectation of the Hamiltonian

$$H_C = \frac{1}{2} \sum_{(i,j)} (Z_{Q_{ri}} \otimes Z_{Q_{rj}} - 1), \quad (17)$$

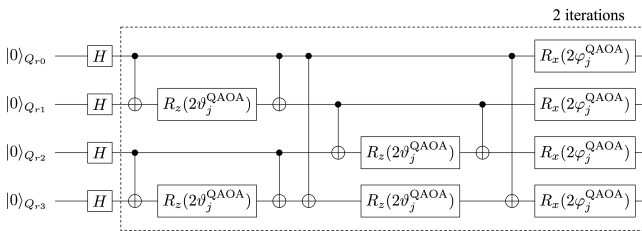


FIG. 15. Quantum circuit for QAOA.

where the symbol (i, j) ($i, j = 0, 1, 2, 3$) denotes the summation for the edges connected by the qubits Q_{ri} and Q_{rj} under the square-graph structure in Fig. 14. In this simulation the physical operator \hat{O} is the Hamiltonian H_C in Eq. (17). The unitary operator for running QAOA, which we denote by U^{QAOA} , consists of three elements. The first one is the unitary operation for creating the reference state and is given by the Hadamard-gate operation on all four qubits, $U_{\text{int}} = H^{\otimes 4}$. The other two are the unitary operations $U_C(\vartheta_j^{\text{QAOA}})$ and $U_X(\varphi_j^{\text{QAOA}})$ which are generated by the Hamiltonian H_C in Eq. (17) with the angle $\vartheta_j^{\text{QAOA}}$ and the term $H_X = \sum_i X_{Q_{ri}}$ with the angle φ_j^{QAOA} , respectively: in QAOA H_X is called the transverse-field (mixing or driving) term. The two types of angles $\vartheta_j^{\text{QAOA}}$ and φ_j^{QAOA} ($j = 1, \dots, p$) are the variational parameters and p is the repetition number of applying the unitary operation $U_X(\varphi_j^{\text{QAOA}}) \cdot U_C(\vartheta_j^{\text{QAOA}})$ (the number of iteration), which determines the accuracy of QAOA. In total, U^{QAOA} is given by

$$U^{\text{QAOA}} = \left[\prod_{j=1}^p \left(U_X(\varphi_j^{\text{QAOA}}) \cdot U_C(\vartheta_j^{\text{QAOA}}) \right) \right] \cdot \left[\bigotimes_{a=0}^3 H_{Q_{ra}} \right], \quad (18)$$

$$U_C(\vartheta_j^{\text{QAOA}}) = e^{-i\vartheta_j^{\text{QAOA}} H_C}, \quad U_X(\varphi_j^{\text{QAOA}}) = e^{-i\varphi_j^{\text{QAOA}} H_X}.$$

The quantum circuit for U^{QAOA} in Eq. (18) is presented in Fig. 15. In our simulation we set $p = 2$ and the circuit depth is $d = 15$. The unitary operation $U_X(\varphi_j^{\text{QAOA}})$ is implemented by the R_x gate (rotation about x axis) with the angle $2\varphi_j^{\text{QAOA}}$. Meanwhile, the quantum circuit for $U_C(\vartheta_j^{\text{QAOA}})$ is composed of the sets of the quantum gates $[U_{CX}[Q_{ri}; Q_{rj}], R_z(2\vartheta_j^{\text{QAOA}})]$, where R_z denotes the rotational gate about z axis and the associated angle is $2\vartheta_j^{\text{QAOA}}$. Corresponding to Eq. (16), the goal of QAOA simulation is to compute and minimize the expectation value

$$C(\vartheta^{\text{QAOA}}, \varphi^{\text{QAOA}}) = \langle \vartheta^{\text{QAOA}}, \varphi^{\text{QAOA}} | H_C | \vartheta^{\text{QAOA}}, \varphi^{\text{QAOA}} \rangle, \quad (19)$$

where $|\vartheta^{\text{QAOA}}, \varphi^{\text{QAOA}}\rangle = U^{\text{QAOA}} |0\rangle^{\otimes 4}$ with $\vartheta^{\text{QAOA}} = (\vartheta_1^{\text{QAOA}}, \vartheta_2^{\text{QAOA}})$ and $\varphi^{\text{QAOA}} = (\varphi_1^{\text{QAOA}}, \varphi_2^{\text{QAOA}})$. Let us also call the expectation value $C(\vartheta^{\text{QAOA}}, \varphi^{\text{QAOA}})$ in Eq. (19) as the cost function and its minimization is equivalent to the optimization of the variational parameters $\vartheta_j^{\text{QAOA}}, \varphi_j^{\text{QAOA}}$, and write them by $\vartheta_j^{\text{QAOA, opt}}, \varphi_j^{\text{QAOA, opt}}$. We show their values in Appendix C. Let us now discuss our simulation results shown in Figs. 16-17. All these results are obtained by computing the probability distribution of the computational basis states since the Hamiltonian H_C in Eq. (17) is given by the Z gate operations. First, let us take a look at the simulation results in Fig. 16. In Fig. 16 (a), we have plotted the results of the cost function $C(\vartheta^{\text{QAOA}}, \varphi^{\text{QAOA}})$ for the ideal simulation ($C_{\text{ideal}} = \langle H_C \rangle_{\rho_{d \dots 1}}$), the noisy simulation ($C_{\text{noisy}} = \langle H_C \rangle_{\rho_{d \dots 1}^{\text{real}}}$), and the simulation with QEM ($C_{\text{QEM}} = \langle H_C \rangle_{\rho_{d \dots 1}^{\text{QEM}}}$). The dashed black line, the blue solid line, and the orange solid line are

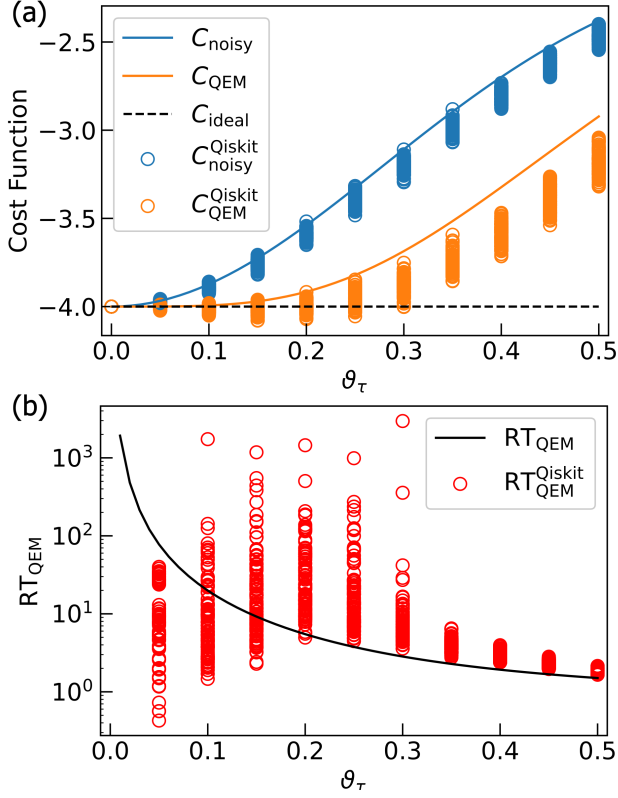


FIG. 16. Quantum simulations for QAOA. In (a) we show the results of QEM for the cost function $C(\vartheta^{\text{QAOA}}, \varphi^{\text{QAOA}})$. The blue and orange solid lines are $C_{\text{noisy}} = \langle H_C \rangle_{\rho_{d \dots 1}^{\text{real}}}$ and $C_{\text{QEM}} = \langle H_C \rangle_{\rho_{d \dots 1}^{\text{QEM}}}$, respectively, and they obtained by our original code. The blue and orange circles are the results of $\langle H_C \rangle_{\rho_{d \dots 1}^{\text{real}}}$ and $\langle H_C \rangle_{\rho_{d \dots 1}^{\text{QEM}}}$ obtained by our Qiskit code, respectively. For this simulation, we have described $\langle H_C \rangle_{\rho_{d \dots 1}^{\text{real}}}$ and $\langle H_C \rangle_{\rho_{d \dots 1}^{\text{QEM}}}$ as $C_{\text{noisy}}^{\text{Qiskit}}$ and $C_{\text{QEM}}^{\text{Qiskit}}$, respectively. The dotted black line is the ideal expectation value $C_{\text{ideal}} = \langle H_C \rangle_{\rho_{d \dots 1}}$. In (b) we have plotted the results of the ratio $\text{RT}_{\text{QEM}}(\vartheta_\tau)$. The black curve is the result obtained by our original code whereas the red circles are the one obtained by our Qiskit code. For each ϑ_τ , we have plotted 100 circles.

C_{ideal} , C_{noisy} , and C_{QEM} , respectively, and they are all obtained by our original code. On the other hand, the blue and orange circles are $\langle H_C \rangle_{\rho_{d \dots 1}^{\text{real}}}$ and $\langle H_C \rangle_{\rho_{d \dots 1}^{\text{QEM}}}$, respectively, and they have been calculated by our Qiskit code. We have denoted $\langle H_C \rangle_{\rho_{d \dots 1}^{\text{real}}}$ and $\langle H_C \rangle_{\rho_{d \dots 1}^{\text{QEM}}}$ by $C_{\text{noisy}}^{\text{Qiskit}}$ and $C_{\text{QEM}}^{\text{Qiskit}}$, respectively. We have plotted 100 circles for each ϑ_τ . We see that in the range $0.1 \leq \vartheta_\tau \leq 0.5$ our QEM works well. In Fig. 16 (b), we have plotted the ratio $\text{RT}_{\text{QEM}}(\vartheta_\tau)$. The black curve is the result obtained by our original code while the red circles are those obtained by our Qiskit code and 100 circles are plotted for each ϑ_τ . Corresponding to the result shown in Fig. 16 (a), the ratio satisfies $\text{RT}_{\text{QEM}}(\vartheta_\tau) > 1$. Finally, let us explain the results in Fig. 17. Here we have presented the histogram of the probability distribution of the computational basis states for the ideal case (P_{ideal}), the noisy case ($P_{\text{noisy}}, P_{\text{noisy}}^{\text{Qiskit}}$), and the case with QEM being performed ($P_{\text{QEM}}, P_{\text{QEM}}^{\text{Qiskit}}$), with set-

ting $\vartheta_\tau = 0.2$. We see that the probabilities of the two quantum states $|0101\rangle$ and $|1010\rangle$ are both equal to 0.5. This implies that under the optimized variational parameters the cost function $C(\vartheta^{\text{QAOA}}, \varphi^{\text{QAOA}})$ becomes minimized such that the four qubits Q_{ri} are partitioned into the two groups $[Q_{r0}, Q_{r2}]$ and $[Q_{r1}, Q_{r3}]$, and it implies that all the edges of the square are to be cut, i.e., the maximum number of edges to be cut is four. Correspondingly, as shown in Fig. 16 (a) the ideal minimum value of the cost function is -4.0 , and we obtain the maximum cut number four by multiplying minus one. Consequently, our QEM scheme works for the noisy QAOA simulation.

D. Discussion for QEM under NISQ Device Parameters

Let us end this section by discussing the validity of our QEM scheme under the conditions of physical parameters of NISQ devices such as gate times and T_1 and T_2 (transverse and longitudinal) times. First, let us discuss the case of superconducting qubit systems. Typically, T_1 times of superconducting qubits are around $100 \mu\text{sec}$ while two-qubit gate times are about 100 nsec [9, 10]. For simplicity, let us set $T_1 = (2\gamma(2\bar{n} + 1))^{-1} \approx (2\gamma)^{-1}$. Here we have taken the qubit frequency and temperature to be 5.0 GHz and 10 mK [8, 16], respectively, and we obtain $\bar{n} \sim 10^{-11}$. Then, the noise strength ϑ_τ is estimated to be $\vartheta_\tau \approx 0.04$. From the results in Figs. 9, 12 and 16, we expect that our QEM works for noisy quantum computing on superconducting-qubit NISQ devices. Next, let us discuss the case of ion-trap qubit systems. For instance, quantum noise effects occurring in hyperfine-state type ion-trap qubit systems are considered to be the phase damping and T_2 times are about 10 sec while two-qubit gate times are about $100 \mu\text{sec}$ [11]. By setting $T_2 = (2\gamma_p)^{-1}$, we have $\tau_p = \gamma_p \Delta t \approx 5 \times 10^{-6}$, which is sufficiently small and therefore, we expect that our QEM scheme also works for ion-trap NISQ devices.

IV. CONCLUSION AND OUTLOOK

In this paper, we have established our QEM scheme for reducing the quantum noise (decoherence) effects on the single-qubit states which occur during the gate operations. We have formulated it as the perturbation theory with respect to the noise strength (in the case of AD effect it is τ), which are evaluated by the gate time and decay rate (T_1 time and/or T_2 time), and is represented by the ensemble of quantum circuits, namely the quantum-noise-effect circuit groups. The numbers of quantum circuits composing the quantum-noise-effect circuit groups are polynomial with respect to the product of the depth of the quantum algorithm under consideration and the number of register bits, which can be considered that the conduction of our QEM scheme is not so high-cost computational performance. To demonstrate the validity of our QEM scheme, we have performed the noisy quantum simulations of the qubits under the AD effects for four types of quantum algorithms based on the linear-order perturbation theory. It is to

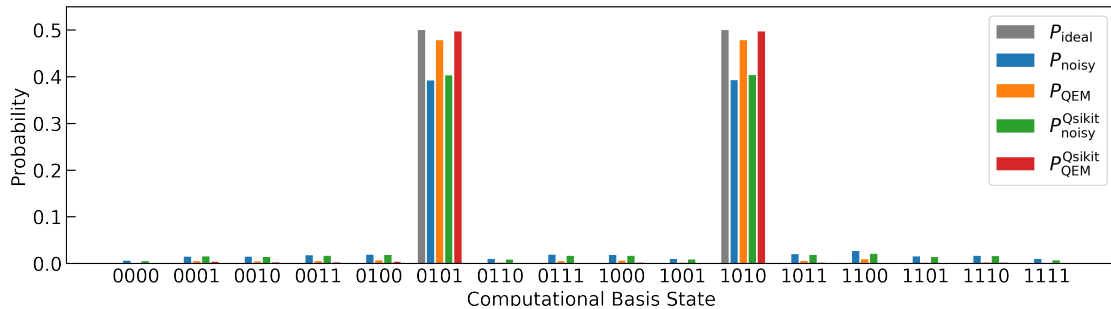


FIG. 17. Histogram of the probability distribution of the computational basis states for QAOA simulations. We have set $\vartheta_\tau = 0.2$. P_{ideal} , P_{noisy} , and $P_{\text{QEM}}^{\text{Qiskit}}$ are obtained by our original code while $P_{\text{noisy}}^{\text{Qiskit}}$ and $P_{\text{QEM}}^{\text{Qiskit}}$ are obtained by the Qiskit code.

be noted that before we conduct our QEM scheme, we need to be careful with if the expectation values on which we are aiming to perform QEM do not include the linear-order term in τ or if they are equivalent to the ideal simulation results like the computation of the expectation value of the identity operator. As long as these two are not the cases then our linear-order QEM scheme works as we have demonstrated in Sec. III and it is valid in a broad region of τ , which implies its effectiveness and powerfulness. Our QEM scheme can be generalized to error mitigation for other types of quantum noises including the generalized amplitude damping, the phase damping, the composition of these two, and the stochastic Pauli noises like the depolarizing channel. Furthermore, it can be extended to cases of error mitigation for higher-order quantum noise effects and once this is established we expect that we become able to perform quantum computations in high accuracy even for long-depth quantum algorithms.

Our QEM scheme is solely conducted by gate operations and measurements on ancilla bits and can be applied to any type of quantum algorithm. Therefore, by using our QEM scheme we become able to programmably perform high-accurate quantum computing solely by the quantum-computational operations (software manipulations) and it can be conducted without having the limitations of the number of qubits and error rates of gate operations. Furthermore, our QEM scheme can be performed with any type of quantum hardware such as solid-state systems and atomic-molecule and optical systems and with quantum devices of any generation. These two characteristics are the big advantages of our scheme. We expect that we become able to obtain quantum computational results with extremely high qualities by combining our QEM scheme with other error-mitigation tasks such as those for state preparation (initialization) and mea-

surement and imperfections of gate operations.

One of the important outlook of this work is quantum computations by large-scale quantum devices or future (next-generation) quantum devices. In such a case, we consider that we also need to take into account quantum noises acting on many-body quantum states such as collective quantum noises [72–74, 82–85] and correlated noises [52, 56, 86–90]. Our QEM scheme can be extended to mitigation of these many-body quantum noise effects provided that they are formulated as groups of quantum circuits. When such formalisms are being constructed, we expect that we become able to realize QEM scheme which mitigates both the single-qubit-state and the many-body-state quantum noise effects. We expect that this leads to conduction of quantum computing for big-size problems with high-quality results being obtained. We believe that this paves the way to realize high-quality quantum computing for application to problems in many branches of science and engineering including material science, quantum chemistry, combinatorial optimization problems, and machine learning using large-scale quantum computers.

ACKNOWLEDGMENTS

We thank all the other members of Quemix Inc. for giving us the fruitful comments and reading this manuscript carefully. This work was supported by MEXT as "Program for Promoting Researches on the Supercomputer Fugaku" (JPMXP1020200205) and JSPS KAKENHI as "Grant-in-Aid for Scientific Research(A)" Grant Number 21H04553. The computation in this work has been done using Supercomputer Center at the Institute for Solid State Physics in the University of Tokyo.

Appendix A: Extended QEM Formalisms

In this section, we discuss extensions of our QEM formalism to various types of quantum noise effects; generalized amplitude damping (GAD), phase damping (PD), and their composite channels. Further, we discuss extensions to cases of higher-order quantum noise effects.

1. QEM for Other Quantum Noises

By taking exactly the same approach for deriving the QEM scheme for the AD effects we can straightforwardly construct our QEM schemes for other quantum noises including GAD, PD, their composite channels, and stochastic Pauli noises. First let us show the case of GAD effects. The quantum master equation for describing the GAD process is given by

$$\frac{\partial \rho(t)}{\partial t} = \gamma \mathcal{L}_{\text{GAD}}[\rho(t)] = \gamma(\bar{n} + 1) \sum_{j=0}^{N_q-1} \left[\tilde{\sigma}_j^- \rho(t) \tilde{\sigma}_j^+ - \frac{1}{2} \{ \tilde{\sigma}_j^+ \tilde{\sigma}_j^-, \rho(t) \} \right] + \gamma \bar{n} \sum_{j=0}^{N_q-1} \left[\tilde{\sigma}_j^+ \rho(t) \tilde{\sigma}_j^- - \frac{1}{2} \{ \tilde{\sigma}_j^- \tilde{\sigma}_j^+, \rho(t) \} \right], \quad (\text{A1})$$

where \mathcal{L}_{GAD} is the Lindblad superoperator of the GAD process and $\bar{n} = (e^{\beta\epsilon} - 1)^{-1}$ is the Bose-Einstein distribution function for the energy ϵ . The quantity β is the inverse temperature. Note that by taking the zero-temperature limit ($\beta \rightarrow \infty$) in Eq. (A1), we obtain the quantum master equation (1). As we did in the case of the AD effect, let us estimate the GAD effect in the first order in τ and write it by $\Delta_1^{\text{GAD}} \rho_{d\dots 1}$ like $\Delta_1^{\text{AD}} \rho_{d\dots 1}$ in Eq. (2). From the quantum master equation (A1), the GAD effect $\Delta_1^{\text{GAD}} \rho_{d\dots 1}$ is evaluated as

$$\begin{aligned} \Delta_1^{\text{GAD}} \rho_{d\dots 1} &= \sum_{k=1}^d \Delta_{1,k}^{\text{GAD}} \rho_{d\dots 1}, \\ \Delta_{1,k}^{\text{GAD}} \rho_{d\dots 1} &= \left(\prod_{l=k+1}^d U_l \right) \cdot \tilde{\rho}_{k\dots 1}^{\text{GAD}} \cdot \left(\prod_{l=k+1}^d U_l \right)^\dagger, \end{aligned} \quad (\text{A2})$$

where

$$\begin{aligned} \tilde{\rho}_{k\dots 1}^{\text{GAD}} &= \mathcal{L}_{\text{GAD}}[\rho_{k\dots 1}] \\ &= \sum_{j=0}^{N_q-1} (\bar{n} + 1) \left[\tilde{\sigma}_j^- \rho_{k\dots 1} \tilde{\sigma}_j^+ - \frac{1}{2} \{ P_j^1, \rho_{k\dots 1} \} \right] \\ &\quad + \bar{n} \left[\tilde{\sigma}_j^+ \rho_{k\dots 1} \tilde{\sigma}_j^- - \frac{1}{2} \{ P_j^0, \rho_{k\dots 1} \} \right] \\ &= (\bar{n} + 1) \tilde{\rho}_{k\dots 1}^{\text{GAD,EM}} + \bar{n} \tilde{\rho}_{k\dots 1}^{\text{GAD,AB}}. \end{aligned} \quad (\text{A3})$$

Physically, the quantity $\tilde{\rho}_{k\dots 1}^{\text{GAD,EM}}$ in the above equation describes emission process of the register bits whereas $\tilde{\rho}_{k\dots 1}^{\text{GAD,AB}}$ represents absorption process. Like Eq. (9), we rewrite these two quantities in terms of the identity operator, Z gate, and the non-unitary operators $\{P^0, P^1, \tilde{\sigma}^\pm\}$. As a result, we have

$$\begin{aligned} \tilde{\rho}_{k\dots 1}^{\text{GAD,EM}} &= \frac{-\rho_{k\dots 1} + Z_j \rho_{k\dots 1} Z_j + \tilde{\sigma}_j^- \rho_{k\dots 1} \tilde{\sigma}_j^+ - P_j^1 \rho_{k\dots 1} P_j^1}{4}, \\ \tilde{\rho}_{k\dots 1}^{\text{GAD,AB}} &= \frac{-\rho_{k\dots 1} + Z_j \rho_{k\dots 1} Z_j + \tilde{\sigma}_j^+ \rho_{k\dots 1} \tilde{\sigma}_j^- - P_j^0 \rho_{k\dots 1} P_j^0}{4}. \end{aligned} \quad (\text{A4})$$

Note that in the zero-temperature limit ($\beta \rightarrow \infty$) we have $\bar{n} \rightarrow 0$ and $\tilde{\rho}_{k\dots 1}^{\text{GAD,EM}} \rightarrow \tilde{\rho}_{k\dots 1}^{\text{AD}}$. By using Eq. (6) with setting $\vartheta = \pi$, the operation of $\tilde{\sigma}_j^+$ can be generated by the AD-effect circuit A with post-selecting the measurement outcome of the

ancilla bit to be $|1\rangle$ while the operation of P_j^0 is created by the AD-effect circuit B with post-selecting the output state $|0\rangle_{Q_a}$. Thus, as in the case of the AD effect, we can perform QEM for GAD by four types of quantum circuits mentioned previously, the original quantum circuit given by U^{QC} , the quantum circuits with the additional Z -gate operations, and the AD-effect circuits A and B. Therefore, the quantum-noise-effect circuit group for GAD effect is equivalent to that for AD effect and the maximum number of the quantum circuits which we need to perform QEM for GAD effect is $3dN_q + 1$. The QEM formula for the GAD effect is given by

$$\langle \hat{O} \rangle_{\rho_{d\dots 1}}^{\text{QEM}} = \langle \hat{O} \rangle_{\rho_{d\dots 1}} + \tau \left(\langle \hat{O} \rangle_{\delta_1^{\text{GAD}}(\rho_{d\dots 1})} - \langle \hat{O} \rangle_{\Delta_1^{\text{GAD}} \rho_{d\dots 1}} \right), \quad (\text{A5})$$

where the symbol δ_1^{GAD} describes the GAD effect on a real device in the first order in τ and

$$\langle \hat{O} \rangle_{\Delta_1^{\text{GAD}} \rho_{d\dots 1}} = (\bar{n} + 1) \langle \hat{O} \rangle_{\Delta_1^{\text{GAD,EM}} \rho_{d\dots 1}} + \bar{n} \langle \hat{O} \rangle_{\Delta_1^{\text{GAD,AB}} \rho_{d\dots 1}}. \quad (\text{A6})$$

Our QEM scheme can also be extended to the case when both GAD and phase damping (PD) occur. The quantum master equation which describes such a process is given by

$$\begin{aligned} \frac{\partial \rho(t)}{\partial t} &= \gamma \mathcal{L}_{\text{GAD}}[\rho(t)] + \gamma_{\text{PD}} \mathcal{L}_{\text{PD}}[\rho(t)] \\ &= \gamma(\bar{n} + 1) \sum_{j=0}^{N_q-1} \left[\tilde{\sigma}_j^- \rho(t) \tilde{\sigma}_j^+ - \frac{1}{2} \{ \tilde{\sigma}_j^+ \tilde{\sigma}_j^-, \rho(t) \} \right] \\ &\quad + \gamma \bar{n} \sum_{j=0}^{N_q-1} \left[\tilde{\sigma}_j^+ \rho(t) \tilde{\sigma}_j^- - \frac{1}{2} \{ \tilde{\sigma}_j^- \tilde{\sigma}_j^+, \rho(t) \} \right] \\ &\quad + \gamma_{\text{PD}} \sum_{j=0}^{N_q-1} [Z_j \rho(t) Z_j - \rho(t)], \end{aligned} \quad (\text{A7})$$

where \mathcal{L}_{PD} is the Lindblad superoperator of PD process and γ_{PD} is the strength of PD. We introduce the dimensionless quantity defined by $\tau_{\text{PD}} = \gamma_{\text{PD}} \cdot \Delta t$ and assume to be in the same order as τ . Like Eq. (2), we represent the solution of quantum master equation (A7) as the perturbative series of τ

and τ_{PD} given by

$$\begin{aligned} \rho(T) &= \rho_{d\cdots 1} + \tau \Delta_1^{\text{GAD}} \rho_{d\cdots 1} + \tau_{\text{PD}} \Delta_1^{\text{PD}} \rho_{d\cdots 1} \\ &+ \mathcal{O}(\tau^2, \tau_{\text{PD}}^2, \tau \tau_{\text{PD}}), \end{aligned} \quad (\text{A8})$$

where $\Delta_1^{\text{PD}} \rho_{d\cdots 1}$ is

$$\begin{aligned} \Delta_1^{\text{PD}} \rho_{d\cdots 1} &= \sum_{k=1}^d \Delta_{1,k}^{\text{PD}} \rho_{d\cdots 1}, \\ \Delta_{1,k}^{\text{PD}} \rho_{d\cdots 1} &= \left(\prod_{l=k+1}^d U_l \right) \tilde{\rho}_{k\cdots 1}^{\text{PD}} \left(\prod_{l=k+1}^d U_l \right)^\dagger, \\ \tilde{\rho}_{k\cdots 1}^{\text{PD}} &= \mathcal{L}_{\text{PD}}[\rho_{k\cdots 1}] = \sum_{j=0}^{N_q-1} Z_j \rho_{k\cdots 1} Z_j - \rho_{k\cdots 1}. \end{aligned} \quad (\text{A9})$$

As we see in the above equation, to evaluate $\Delta_1^{\text{PD}} \rho_{d\cdots 1}$ the only additional operation which we need is the Z -gate operation. Therefore, the quantum-noise-effect circuit group for the composite channel of the GAD and PD effects is equivalent to that of GAD (AD) effect. Let us denote the composition of the GAD and PD effects which occur on a real device by the symbol $\delta^{\text{GAD-PD}}$. In the first-order approximation with respect to τ and τ_{PD} we can express $\delta^{\text{GAD-PD}}(\rho_{d\cdots 1})$ as $\delta^{\text{GAD-PD}}(\rho_{d\cdots 1}) = \tau \delta_1^{\text{GAD}}(\rho_{d\cdots 1}) + \tau_{\text{PD}} \delta_1^{\text{PD}}(\rho_{d\cdots 1})$. Our QEM formula is given by

$$\begin{aligned} \langle \hat{O} \rangle_{\rho_{d\cdots 1}}^{\text{QEM}} &\equiv \langle \hat{O} \rangle_{\rho_{d\cdots 1}^{\text{real}}} - \tau \langle \hat{O} \rangle_{(\Delta_1^{\text{GAD}} \rho_{d\cdots 1})^{\text{real}}} - \tau_{\text{PD}} \langle \hat{O} \rangle_{(\Delta_1^{\text{PD}} \rho_{d\cdots 1})^{\text{real}}} \\ &= \langle \hat{O} \rangle_{\rho_{d\cdots 1}} + \tau \left(\langle \hat{O} \rangle_{\delta_1^{\text{GAD}}(\rho_{d\cdots 1})} - \langle \hat{O} \rangle_{\Delta_1^{\text{GAD}} \rho_{d\cdots 1}} \right) + \tau_{\text{PD}} \left(\langle \hat{O} \rangle_{\delta_1^{\text{PD}}(\rho_{d\cdots 1})} - \langle \hat{O} \rangle_{\Delta_1^{\text{PD}} \rho_{d\cdots 1}} \right) + \mathcal{O}(\tau^2), \end{aligned} \quad (\text{A10})$$

We end this section by noting that our QEM scheme can be extended to the mitigation of stochastic Pauli noise effects (bit flip, phase flip, bit-phase flip, depolarizing channel): Here we do not show detailed analysis for them. Likewise the PD effect, the stochastic Pauli noise effects are represented by the identity operator and X, Y , and Z gates. For these cases, to conduct QEM we just need to prepare quantum circuits composed with additional X, Y , and Z gate operations like $\sum_{j=0}^{N_q-1} Z_j \rho_{k\cdots 1} Z_j$ in Eq. (9) and the ancilla bits are not needed.

2. QEM for Higher-Order AD Effects

When a quantum state at a time t_0 , which we denote by $\rho(t_0)$, is subject to the AD effect during the time interval Δt , according to the quantum master equation (1) the quantum state at the time $t = t_0 + \Delta t$ is given by $\rho(t_0 + \Delta t) = \rho(t_0) +$

$\mathcal{L}_{\text{AD}}[\rho(t_0)]\tau + \mathcal{L}_{\text{AD}}^2[\rho(t_0)]\frac{\tau^2}{2!} + \mathcal{O}(\tau^3)$. Here $\mathcal{L}_{\text{AD}}^2$ describes the twice operation of \mathcal{L}_{AD} and it is equivalent to the second-order time derivative obeying the quantum master equation (1). In other words, we have solved the quantum master equation (2) up to the second order in Δt . Let us analyze the quantum state generated by the unitary operation $U^{\text{QC}} = \prod_{k=1}^d U_k = U_d \cdot U_{d-1} \cdots U_2 \cdot U_1$ under the influence of the AD effect and write it by $\rho(T)$. As similar to the second line of the right-hand side of Eq. (2), up to $\mathcal{O}(\tau^2)$ the density matrix $\rho(T)$ is calculated as

$$\rho(T) = \rho_{d\cdots 1} + \tau \Delta_1^{\text{AD}} \rho_{d\cdots 1} + \frac{\tau^2}{2!} \Delta_2^{\text{AD}} \rho_{d\cdots 1} + \mathcal{O}(\tau^3), \quad (\text{A11})$$

where $\Delta_2^{\text{AD}} \rho_{d\cdots 1}$ denotes the theoretically-evaluated second-order AD effect associated with the unitary operation U^{QC} and is given by

$$\begin{aligned}
\Delta_2 \rho_{d \dots 1} &= \frac{1}{2} \sum_{j_1, j_2=0}^{N_q-1} \mathcal{L}_{j_1}^{\text{AD}} [\mathcal{L}_{j_2}^{\text{AD}} [\rho_{d \dots 1}]] + \frac{1}{2} \sum_{k=1}^{d-1} \sum_{j_1, j_2=0}^{N_q-1} \left(\prod_{l=k+1}^d U_l \right) \mathcal{L}_{j_1}^{\text{AD}} [\mathcal{L}_{j_2}^{\text{AD}} [\rho_{k \dots 1}]] \left(\prod_{l=k+1}^d U_l \right)^\dagger \\
&+ \sum_{k=1}^{d-1} \sum_{j_1, j_2=0}^{N_q-1} \mathcal{L}_{j_1}^{\text{AD}} \left[\left(\prod_{l=k+1}^d U_l \right) \mathcal{L}_{j_2}^{\text{AD}} [\rho_{k \dots 1}] \left(\prod_{l=k+1}^d U_l \right)^\dagger \right] \\
&+ \sum_{k_1=2}^{d-1} \sum_{k_2=2}^{k_1-1} \sum_{k_1=2}^{d-1} \sum_{k_2=1}^{k_1} \sum_{j_1, j_2=0}^{N_q-1} \left(\prod_{l_1=k_1+1}^d U_{l_1} \right) \mathcal{L}_{j_1}^{\text{AD}} \left[\left(\prod_{l_2=k_2+1}^{k_1} U_{l_2} \right) \mathcal{L}_{j_2}^{\text{AD}} [\rho_{k_2 \dots 1}] \left(\prod_{l_2=k_2+1}^{k_1} U_{l_2} \right)^\dagger \right] \left(\prod_{l_1=k_1+1}^d U_{l_1} \right)^\dagger.
\end{aligned} \tag{A12}$$

We note that the two terms in the first line of the right-hand side of the above equation includes the second-order deriva-

tive terms of τ and they are obtained when $j_1 = j_2$. By using Eq. (9), $\Delta_2 \rho_{d \dots 1}$ in Eq. (A12) is represented by the operators $\{\mathbf{1}_{2 \times 2}, Z, \tilde{\sigma}^\pm, P^1\}$ as

$$\begin{aligned}
\Delta_2 \rho_{d \dots 1} &= \frac{1}{2} \sum_{j_1, j_2}^{N_q-1} \sum_{p_1, p_2} c_{p_1} c_{p_2} s_{Q_{j_1}, p_1} s_{Q_{j_2}, p_2} \rho_{d \dots 1} s_{Q_{j_2}, p_2}^\dagger s_{Q_{j_1}, p_1}^\dagger \\
&+ \frac{1}{2} \sum_{k=1}^{d-1} \sum_{j_1, j_2}^{N_q-1} \sum_{p_1, p_2} c_{p_1} c_{p_2} \left(\prod_{l=k+1}^d U_l \right) s_{Q_{j_1}, p_1} s_{Q_{j_2}, p_2} \rho_{k \dots 1} s_{Q_{j_2}, p_2}^\dagger s_{Q_{j_1}, p_1}^\dagger \left(\prod_{l=k+1}^d U_l \right)^\dagger \\
&+ \sum_{k=1}^{d-1} \sum_{j_1, j_2}^{N_q-1} \sum_{p_1, p_2} c_{p_1} c_{p_2} s_{Q_{j_1}, p_1} \left[\left(\prod_{l=k+1}^d U_l \right) s_{Q_{j_2}, p_2} \rho_{k \dots 1} s_{Q_{j_2}, p_2}^\dagger \left(\prod_{l=k+1}^d U_l \right)^\dagger \right] s_{Q_{j_1}, p_1}^\dagger \\
&+ \sum_{k_1=2}^{d-1} \sum_{k_2=2}^{k_1-1} \sum_{k_1=2}^{d-1} \sum_{k_2=1}^{k_1} \sum_{j_1, j_2}^{N_q-1} \sum_{p_1, p_2} c_{p_1} c_{p_2} \left(\prod_{l_1=k_1+1}^d U_{l_1} \right) s_{Q_{j_1}, p_1} \left(\prod_{l_2=k_2+1}^{k_1} U_{l_2} \right) s_{Q_{j_2}, p_2} \rho_{k_2 \dots 1} \\
&\times s_{Q_{j_2}, p_2}^\dagger \left(\prod_{l_2=k_2+1}^{k_1} U_{l_2} \right)^\dagger s_{Q_{j_1}, p_1}^\dagger \left(\prod_{l_1=k_1+1}^d U_{l_1} \right)^\dagger,
\end{aligned} \tag{A13}$$

where the subscripts p_1 and p_2 are used for labeling the four operators $\{\mathbf{1}_{2 \times 2}, Z, \tilde{\sigma}^\pm, P^1\}$, and correspondingly, $s_{Q_{j_a}, p_a}$ ($a = 1, 2$) is the operator acting on the qubit Q_{j_a} and $s_{Q_{j_a}, p_a} \in \{\mathbf{1}_{2 \times 2, j_a}, Z_{j_a}, \tilde{\sigma}_{j_a}^\pm, P_{j_a}^1\}$. For instance, $s_{Q_{j_a}, Z}$ is the Z -gate operation acting on the qubit Q_{j_a} . The coefficient c_{p_a} ($a = 1, 2$) is assigned when the operator $s_{Q_{j_a}, p_a}$ is acted on the qubit Q_{j_a} . The explicit form of the coefficients c_{p_a} are $\{c_{\mathbf{1}_{2 \times 2}}, c_Z, c_{\tilde{\sigma}^-}, c_{P^1}\} = \{-\frac{1}{4}, \frac{1}{4}, 1, -1\}$. To derive Eq. (A13) we have used the relations

$$\begin{aligned}
Z \tilde{\sigma}^\mp &= \pm \tilde{\sigma}^\mp, & \tilde{\sigma}^\mp Z &= \mp \tilde{\sigma}^\mp, \\
\tilde{\sigma}^+ P^1 &= P^1 \tilde{\sigma}^- = 0, & \tilde{\sigma}^- P^1 &= \tilde{\sigma}^-, & P^1 \tilde{\sigma}^+ &= \tilde{\sigma}^+, \\
P^1 Z &= Z P^1 = -P^1.
\end{aligned} \tag{A14}$$

By representing the second-order effect $\Delta_2 \rho_{d \dots 1}$ in the way given in Eq. (A13), we can programmably evaluate $\Delta_2 \rho_{d \dots 1}$ by the unitary operators U_l ($l = 1, \dots, d$) which compose the quantum algorithm under consideration, the additional operations $s_{Q_{j_a}, p_a} \in \{\mathbf{1}_{2 \times 2}, Z, \tilde{\sigma}^\pm, P^1\}$, and the coefficients $c_{p_a} \in \{-\frac{1}{4}, \frac{1}{4}, 1, -1\}$. In other words, we can create the AD-effect (quantum-noise-effect) circuit group for evaluating $\Delta_2 \rho_{d \dots 1}$. Note that the quantum circuits for evaluating the terms in the first and second lines of Eq. (A13) is equivalent to the AD-effect-circuit group for evaluating $\Delta_1 \rho_{d \dots 1}$ for $j_1 = j_2$. By using Eq. (8), we can derive the formula of QEM for the second-order AD effect and is given by

$$\begin{aligned}
\langle \hat{O} \rangle_{\rho_{d\dots 1}}^{\text{QEM}} &\equiv \langle \hat{O} \rangle_{\rho_{d\dots 1}^{\text{real}}} - \tau \langle \hat{O} \rangle_{(\Delta_1^{\text{AD}} \rho_{d\dots 1})^{\text{real}}} - \frac{\tau^2}{2!} \langle \hat{O} \rangle_{(\Delta_1^{\text{AD}} \rho_{d\dots 1})^{\text{real}}} + \tau^2 \langle \hat{O} \rangle_{\Delta_1^{\text{AD}}((\Delta_1^{\text{AD}} \rho_{d\dots 1}))^{\text{real}}} \\
&= \langle \hat{O} \rangle_{\rho_{d\dots 1}} + \tau \left(\langle \hat{O} \rangle_{\delta_1^{\text{AD}}(\rho_{d\dots 1})} - \langle \hat{O} \rangle_{\Delta_1^{\text{AD}} \rho_{d\dots 1}} \right) \\
&+ \frac{\tau^2}{2!} \left(\langle \hat{O} \rangle_{\delta_2^{\text{AD}}(\rho_{d\dots 1})} - \langle \hat{O} \rangle_{\Delta_2^{\text{AD}} \rho_{d\dots 1}} \right) - \tau^2 \left(\langle \hat{O} \rangle_{\delta_1^{\text{AD}}((\Delta_1^{\text{AD}} \rho_{d\dots 1}))} - \langle \hat{O} \rangle_{\Delta_1^{\text{AD}}((\Delta_1^{\text{AD}} \rho_{d\dots 1}))} \right) + \mathcal{O}(\tau^3). \tag{A15}
\end{aligned}$$

The first term in the second line of the right-hand side of the above equation is the ideal expectation value while the second term describes the QEM for the first-order AD effect; compare with Eq. (8). On the other hand, the terms in the third line of the right-hand side describes the conduction of the QEM for the second-order AD effect. The first term describes the QEM for the intrinsic second-order AD effect while the second term describes the mitigation for the first-order AD effect $\delta_1^{\text{AD}}((\Delta_1^{\text{AD}} \rho_{d\dots 1}))$. Such an error has been arose owing to the conduction of the QEM for the first-order AD effect and has been neglected in the first-order perturbation theory. Consequently, we have derived the QEM for the second-order AD effect and is represented by Eq. (A15).

The above argument can be extended into the formulations of QEM schemes for high-order AD effects. By using Eq. (9) with the relations in Eq. (A14), we can evaluate the higher-order AD effects $\Delta_p^{\text{AD}} \rho_{d\dots 1}$ ($p \geq 3$) and represented them in programmable ways in terms of the operators $\{\mathbf{1}_{2 \times 2}, Z, \tilde{\sigma}^\mp, P^1\}$ like Eq. (A13) and create p -th-order quantum-noise circuit groups. Then we can derive the QEM formula for the higher-order AD effects $\delta_p^{\text{AD}} \rho_{d\dots 1}$. In order to do this, we need to evaluate not only $\Delta_p^{\text{AD}} \rho_{d\dots 1}$ but also $\Delta_k^{\text{AD}}(\Delta_{p-k}^{\text{AD}} \rho_{d\dots 1})$ such that $1 \leq k < p$, which is coming from the conduction of QEM for k -th order AD effects $\delta_k^{\text{AD}} \rho_{d\dots 1}(\Delta_{p-k}^{\text{AD}} \rho_{d\dots 1})$. Furthermore, by applying the argument given above we can construct QEM formulas for higher-order effects of GAD, PD, their mixture, and the stochastic Pauli noises.

For evaluating the second-order effect $\Delta_2 \rho_{d\dots 1}$, we perform the additional operators $\{Z, \sigma^\pm, P^0, P^1\}$ twice as shown in Eq. (A13) and the number of additional quantum circuits to create a second-order AD-effect quantum circuit group is $\mathcal{O}(\{dN_q\}^2)$ and maximally we need two ancilla bits. Similarly, in the case of p -th order AD-effect circuit groups, we need to perform p additional operations of $\{Z, \sigma^\pm, P^0, P^1\}$, and correspondingly, we obtain the additional quantum circuits whose number is $\mathcal{O}(\{dN_q\}^p)$. Furthermore, we need maximally p ancilla bits. Note that for $p \geq N_q$, the maximum number of ancilla bits we need is N_q due to Eq. (A14).

Appendix B: Quantum Circuits for O_{QAA}

In Fig. 18, we show the quantum circuit for O_{QAA} [32]

Appendix C: Variational Parameters for QAOA

We list the optimized numerical values of the variational parameters of QAOA which are given by

$$\begin{aligned}
\vartheta_0^{\text{QAOA}} &= 2.023075, \\
\vartheta_1^{\text{QAOA}} &= 2.130055, \\
\varphi_0^{\text{QAOA}} &= 1.011537, \\
\varphi_1^{\text{QAOA}} &= 1.118518. \tag{C1}
\end{aligned}$$

[1] R. P. Feynman, International Journal of Theoretical Physics **21** (1982).
[2] D. Deutsch, Proceedings of the Royal Society of London. A, Mathematical and Physical Sciences **400**, 97 (1985).
[3] S. Lloyd, Science, 1073 (1996).
[4] D. P. DiVincenzo, Fortschritte der Physik: Progress of Physics **48**, 771 (2000).
[5] M. A. Nielsen and I. Chuang, Quantum computation and quantum information (2002).
[6] I. M. Georgescu, S. Ashhab, and F. Nori, Rev. Mod. Phys. **86**, 153 (2014).
[7] G. Wendin, Reports on Progress in Physics **80**, 106001 (2017).
[8] P. Krantz, M. Kjaergaard, F. Yan, T. P. Orlando, S. Gustavsson, and W. D. Oliver, Applied Physics Reviews **6**, 021318 (2019).
[9] M. Kjaergaard, M. E. Schwartz, J. Braumüller, P. Krantz, J. I-

J. Wang, S. Gustavsson, and W. D. Oliver, Annual Review of Condensed Matter Physics **11**, 369 (2020).
[10] H.-L. Huang, D. Wu, D. Fan, and X. Zhu, Science China Information Sciences **63**, 1 (2020).
[11] C. D. Bruzewicz, J. Chiaverini, R. McConnell, and J. M. Sage, Applied Physics Reviews **6**, 021314 (2019).
[12] V. Kaushal, B. Lekitsch, A. Stahl, J. Hilder, D. Pijn, C. Schmiegelow, A. Bermudez, M. Müller, F. Schmidt-Kaler, and U. Poschinger, AVS Quantum Science **2**, 014101 (2020).
[13] Y. Nakamura, Y. A. Pashkin, and J. Tsai, nature **398**, 786 (1999).
[14] Y. Makhlin, G. Schön, and A. Shnirman, Rev. Mod. Phys. **73**, 357 (2001).
[15] Z.-L. Xiang, S. Ashhab, J. Q. You, and F. Nori, Rev. Mod. Phys. **85**, 623 (2013).

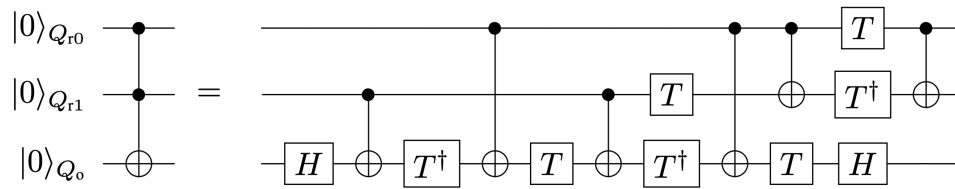


FIG. 18. Quantum circuits for U^{QAA} in Eq. (14).

- [16] S. Kwon, A. Tomonaga, G. Lakshmi Bhai, S. J. Devitt, and J.-S. Tsai, *Journal of Applied Physics* **129**, 041102 (2021).
- [17] J. I. Cirac and P. Zoller, *Phys. Rev. Lett.* **74**, 4091 (1995).
- [18] A. Sørensen and K. Mølmer, *Phys. Rev. Lett.* **82**, 1971 (1999).
- [19] D. Leibfried, R. Blatt, C. Monroe, and D. Wineland, *Rev. Mod. Phys.* **75**, 281 (2003).
- [20] D. J. Wineland, *Physica Scripta* **2009**, 014007 (2009).
- [21] H. Häffner, C. F. Roos, and R. Blatt, *Physics reports* **469**, 155 (2008).
- [22] A. Peruzzo, J. McClean, P. Shadbolt, M.-H. Yung, X.-Q. Zhou, P. J. Love, A. Aspuru-Guzik, and J. L. O'Brien, *Nature communications* **5**, 1 (2014).
- [23] J. R. McClean, J. Romero, R. Babbush, and A. Aspuru-Guzik, *New Journal of Physics* **18**, 023023 (2016).
- [24] A. Kandala, A. Mezzacapo, K. Temme, M. Takita, M. Brink, J. M. Chow, and J. M. Gambetta, *Nature* **549**, 242 (2017).
- [25] S. McArdle, S. Endo, A. Aspuru-Guzik, S. C. Benjamin, and X. Yuan, *Rev. Mod. Phys.* **92**, 015003 (2020).
- [26] S. Endo, Z. Cai, S. C. Benjamin, and X. Yuan, *Journal of the Physical Society of Japan* **90**, 032001 (2021).
- [27] E. Farhi, J. Goldstone, and S. Gutmann, *arXiv preprint arXiv:1411.4028* (2014).
- [28] G. E. Crooks, *arXiv preprint arXiv:1811.08419* (2018).
- [29] Z. Wang, S. Hadfield, Z. Jiang, and E. G. Rieffel, *Physical Review A* **97**, 022304 (2018).
- [30] R. Shaydulin and Y. Alexeev, in *2019 tenth international green and sustainable computing conference (IEEE, 2019)* pp. 1–6.
- [31] L. Zhou, S.-T. Wang, S. Choi, H. Pichler, and M. D. Lukin, *Physical Review X* **10**, 021067 (2020).
- [32] J. Abhijith, A. Adedoyin, J. Ambrosiano, P. Anisimov, A. Bäertschi, W. Casper, G. Chennupati, C. Coffrin, H. Djidjev, D. Gunter, et al., *arXiv e-prints*, *arXiv* (2018).
- [33] M. Schuld and F. Petruccione, *Supervised learning with quantum computers*, Vol. 17 (Springer, 2018).
- [34] K. Mitarai, M. Negoro, M. Kitagawa, and K. Fujii, *Phys. Rev. A* **98**, 032309 (2018).
- [35] M. Benedetti, E. Lloyd, S. Sack, and M. Fiorentini, *Quantum Science and Technology* **5**, 019601 (2019).
- [36] F. Arute, K. Arya, R. Babbush, D. Bacon, J. C. Bardin, R. Barends, R. Biswas, S. Boixo, F. G. Brandao, D. A. Buell, et al., *Nature* **574**, 505 (2019).
- [37] J. Preskill, *Quantum* **2**, 79 (2018).
- [38] G. Palma and K. Suominen, *London A* **452**, 567 (1996).
- [39] S. Resch and U. Karpuzcu, *arXiv preprint arXiv:1912.00546*.
- [40] P. W. Shor, *Phys. Rev. A* **52**, R2493 (1995).
- [41] S. J. Devitt, W. J. Munro, and K. Nemoto, *Reports on Progress in Physics* **76**, 076001 (2013).
- [42] D. A. Lidar and T. A. Brun, *Quantum error correction* (Cambridge university press, 2013).
- [43] J. Roffe, *Contemporary Physics* **60**, 226 (2019).
- [44] L. Viola and S. Lloyd, *Physical Review A* **58**, 2733 (1998).
- [45] L. Viola, E. Knill, and S. Lloyd, *Physical Review Letters* **82**, 2417 (1999).
- [46] K. Khodjasteh and D. A. Lidar, *Physical review letters* **95**, 180501 (2005).
- [47] Y. Masuyama, K. Mizuno, H. Ozawa, H. Ishiwata, Y. Hatano, T. Ohshima, T. Iwasaki, and M. Hatano, *Review of Scientific Instruments* **89**, 125007 (2018).
- [48] K. Temme, S. Bravyi, and J. M. Gambetta, *Physical review letters* **119**, 180509 (2017).
- [49] A. Kandala, K. Temme, A. D. Córcoles, A. Mezzacapo, J. M. Chow, and J. M. Gambetta, *Nature* **567**, 491 (2019).
- [50] Y. Li and S. C. Benjamin, *Physical Review X* **7**, 021050 (2017).
- [51] S. Endo, S. C. Benjamin, and Y. Li, *Physical Review X* **8**, 031027 (2018).
- [52] V. N. Premakumar and R. Joynt, *arXiv preprint arXiv:1812.07076* (2018).
- [53] X. Bonet-Monroig, R. Sagastizabal, M. Singh, and T. O'Brien, *Physical Review A* **98**, 062339 (2018).
- [54] S. McArdle, X. Yuan, and S. Benjamin, *Physical review letters* **122**, 180501 (2019).
- [55] A. Zlokapa and A. Gheorghiu, *arXiv preprint arXiv:2005.10811* (2020).
- [56] S. Bravyi, S. Sheldon, A. Kandala, D. C. McKay, and J. M. Gambetta, *Phys. Rev. A* **103**, 042605 (2021).
- [57] J. Sun, X. Yuan, T. Tsunoda, V. Vedral, S. C. Benjamin, and S. Endo, *Phys. Rev. Applied* **15**, 034026 (2021).
- [58] M. Otten and S. K. Gray, *npj Quantum Information* **5**, 1 (2019).
- [59] M. Otten and S. K. Gray, *Phys. Rev. A* **99**, 012338 (2019).
- [60] J. R. McClean, M. E. Kimchi-Schwartz, J. Carter, and W. A. de Jong, *Phys. Rev. A* **95**, 042308 (2017).
- [61] P. Czarnik, A. Arrasmith, P. J. Coles, and L. Cincio, *Quantum* **5**, 592 (2021).
- [62] A. Strikis, D. Qin, Y. Chen, S. C. Benjamin, and Y. Li, *PRX Quantum* **2**, 040330 (2021).
- [63] W. J. Huggins, S. McArdle, T. E. O'Brien, J. Lee, N. C. Rubin, S. Boixo, K. B. Whaley, R. Babbush, and J. R. McClean, *Phys. Rev. X* **11**, 041036 (2021).
- [64] B. Koczor, *Physical Review X* **11**, 031057 (2021).
- [65] H. Wang, S. Ashhab, and F. Nori, *Phys. Rev. A* **83**, 062317 (2011).
- [66] Z. Hu, R. Xia, and S. Kais, *Scientific reports* **10**, 1 (2020).
- [67] S. Tornow, W. Gehrke, and U. Helmbrecht, *arXiv preprint arXiv:2011.11059* (2020).
- [68] G. García-Pérez, M. A. Rossi, and S. Maniscalco, *npj Quantum Information* **6**, 1 (2020).
- [69] L. Del Re, B. Rost, A. F. Kemper, and J. K. Freericks, *Phys. Rev. B* **102**, 125112 (2020).
- [70] M. Koppenhöfer, C. Bruder, and A. Roulet, *Physical Review Research* **2**, 023026 (2020).
- [71] W. A. de Jong, M. Metcalf, J. Mulligan, M. Płoskoń, F. Ringer, and X. Yao, *Physical Review D* **104**, L051501 (2021).
- [72] H. J. Carmichael, *Statistical methods in quantum optics I: master equations* Vol. 1 (Springer Science & Business Media, 1999).

- [73] G. S. Agarwal, *Quantum optics* (Cambridge University Press, 2012).
- [74] H.-P. Breuer, F. Petruccione, et al., *The theory of open quantum systems* (Oxford University Press on Demand, 2002).
- [75] K. Kraus, A. Böhm, J. D. Dollard, and W. Wootters, *Lecture notes in physics* **190** (1983).
- [76] H. Abraham, AduOffei, R. Agarwal, I. Y. Akhalwaya, G. Aleksandrowicz, T. Alexander, M. Amy, E. Arbel, Arijit02, A. Asfaw, A. Avkhadiev, C. Azaustre, AzizNgoueya, A. Banerjee, A. Bansal, P. Barkoutsos, A. Barnawal, G. Barron, G. S. Barron, L. Bello, Y. Ben-Haim, D. Bevenius, A. Bhubhe, L. S. Bishop, C. Blank, S. Bolos, S. Bosch, Brandon, S. Bravyi, Bryce-Fuller, D. Bucher, A. Burov, F. Cabrera, P. Calpin, L. Capelluto, J. Carballo, G. Carrascal, A. Chen, C.-F. Chen, E. Chen, J. C. Chen, R. Chen, J. M. Chow, S. Churchill, C. Claus, C. Clauss, R. Cocking, F. Correa, A. J. Cross, A. W. Cross, S. Cross, J. Cruz-Benito, C. Culver, A. D. Córcoles-Gonzales, S. Dague, T. E. Dandachi, M. Daniels, M. Dartiailh, DavideFrr, A. R. Davila, A. Dekusar, D. Ding, J. Doi, E. Drechsler, Drew, E. Dumitrescu, K. Dumon, I. Duran, K. EL-Safty, E. Eastman, G. Eberle, P. Eendebak, D. Egger, M. Everitt, P. M. Fernández, A. H. Ferrera, R. Fouilland, FranckChevallier, A. Frisch, A. Fuhrer, B. Fuller, M. GEORGE, J. Gacon, B. G. Gago, C. Gambella, J. M. Gambetta, A. Gammanpila, L. Garcia, T. Garg, S. Garion, A. Gilliam, A. Giridharan, J. Gomez-Mosquera, Gonzalo, S. de la Puente González, J. Gorzinski, I. Gould, D. Greenberg, D. Grinko, W. Guan, J. A. Gunnels, M. Haglund, I. Haide, I. Hamamura, O. C. Hamido, F. Harkins, V. Havlicek, J. Hellmers, L. Herok, S. Hillmich, H. Horii, C. Howington, S. Hu, W. Hu, J. Huang, R. Huisman, H. Imai, T. Imamichi, K. Ishizaki, R. Iten, T. Itoko, JamesSeaward, A. Javadi, A. Javadi-Abhari, W. Javed, Jessica, M. Jivrajani, K. Johns, S. Johnstun, Jonathan-Shoemaker, V. K, T. Kachmann, A. Kale, N. Kanazawa, Kang-Bae, A. Karazeev, P. Kassebaum, J. Kelso, S. King, Knabberjoe, Y. Kobayashi, A. Kovyrshin, R. Krishnakumar, V. Krishnan, K. Krsulich, P. Kumkar, G. Kus, R. LaRose, E. Lacal, R. Lambert, J. Lapeyre, J. Latone, S. Lawrence, C. Lee, G. Li, D. Liu, P. Liu, Y. Maeng, K. Majmudar, A. Malyshev, J. Manela, J. Marecek, M. Marques, D. Maslov, D. Mathews, A. Matsuo, D. T. McClure, C. McGarry, D. McKay, D. McPherson, S. Meesala, T. Metcalfe, M. Mevissen, A. Meyer, A. Mezzacapo, R. Midha, Z. Mineev, A. Mitchell, N. Moll, J. Montanez, G. Monteiro, M. D. Mooring, R. Morales, N. Moran, M. Motta, MrF, P. Murali, J. Müggenburg, D. Nadlinger, K. Nakanishi, G. Nannicini, P. Nation, E. Navarro, Y. Naveh, S. W. Neagle, P. Neuweiler, J. Nicander, P. Niroula, H. Norlen, NuoWenLei, L. J. O’Riordan, O. Ogunbayo, P. Ollitrault, R. Otaolea, S. Oud, D. Padilha, H. Paik, S. Pal, Y. Pang, V. R. Pasquozzi, S. Perriello, A. Phan, F. Piro, M. Pistoia, C. Piveteau, P. Pocreau, A. Pozas-Kerstjens, M. Prokop, V. Prutyaynov, D. Puzzuoli, J. Pérez, Quintiii, R. I. Rahman, A. Raja, N. Ramagiri, A. Rao, R. Raymond, R. M.-C. Redondo, M. Reuter, J. Rice, M. Riedemann, M. L. Rocca, D. M. Rodríguez, RohithKarur, M. Rossmannek, M. Ryu, T. SAPV, SamFerracin, M. Sandberg, H. Sandesara, R. Sapra, H. Sargsyan, A. Sarkar, N. Sathaye, B. Schmitt, C. Schnabel, Z. Schoenfeld, T. L. Scholten, E. Schoute, J. Schwarm, I. F. Sertage, K. Setia, N. Shammah, Y. Shi, A. Silva, A. Simonetto, N. Singstock, Y. Siraichi, I. Sirdikov, S. Sivarajah, M. B. Sletfjerd- ing, J. A. Smolin, M. Soeken, I. O. Sokolov, I. Sokolov, SooluThomas, Starfish, D. Steenzen, M. Stypulkoski, S. Sun, K. J. Sung, H. Takahashi, T. Takawale, I. Tavernelli, C. Taylor, P. Taylour, S. Thomas, M. Tillet, M. Tod, M. Tomasik, E. de la Torre, K. Trabing, M. Treinish, TrishaPe, D. Tuls, W. Turner, Y. Vaknin, C. R. Valcarce, F. Varchon, A. C. Vazquez, V. Villar, D. Vogt-Lee, C. Vuillot, J. Weaver, J. Weidenfeller, R. Wiczorek, J. A. Wildstrom, E. Winston, J. J. Woehr, S. Woerner, R. Woo, C. J. Wood, R. Wood, S. Wood, S. Wood, J. Wootton, D. Yeralin, D. Yonge-Mallo, R. Young, J. Yu, C. Zachow, L. Zdanski, H. Zhang, C. Zoufal, Zoufalc, a kapila, a matsuo, bcamorrison, brandhsn, nick bronn, brosand, chlorophyll zz, csseifms, dekel.meirom, dekelmeirom, dekool, dime10, drholmie, dtrenev, ehchen, elfrocampeador, faisalde- bouni, fanizzamarco, gabrieleagl, gadijal, galeinston, georgios ts, gruu, hhorii, hykavitha, jagunther, jliu45, jscott2, kane- jess, klinvill, krutik2966, kurarr, lerongil, ma5x, merav aha- roni, michelle4654, ordmoj, sagar pahwa, rmoyard, saswati qiskit, scottkelso, sethmerkel, shaashwat, sternparky, strickro- man, sumitpuri, tigerjack, toural, tsura crisaldo, vvilpas, welien, willhbang, yang.luh, yotamvakninibm, and M. Čepulkovskis, [Qiskit: An open-source framework for quantum computing](#) (2019).
- [77] L. K. Grover, *Proceedings of the 28th annual acm symposium on the theory of computing* (1996).
- [78] L. K. Grover, *Phys. Rev. Lett.* **79**, 325 (1997).
- [79] A. Montanaro, *npj Quantum Information* **2**, 1 (2016).
- [80] S. Jordan, Retrieved June 27, 2013 (2011).
- [81] Y. Minato, K. Higa, and R. Nagai, [IBM Quantum de manabu ryoshi konpyuuta \(in Japanese\)](#) (Shuwa System, 2021).
- [82] R. H. Dicke, *Physical review* **93**, 99 (1954).
- [83] M. Gross and S. Haroche, *Physics reports* **93**, 301 (1982).
- [84] L.-M. Duan and G.-C. Guo, *Phys. Rev. A* **58**, 3491 (1998).
- [85] E. M. Fortunato, L. Viola, J. Hodges, G. Teklemariam, and D. G. Cory, *New Journal of Physics* **4**, 5 (2002).
- [86] C. Macchiavello and G. M. Palma, *Phys. Rev. A* **65**, 050301 (2002).
- [87] Y. Yeo and A. Skeen, *Phys. Rev. A* **67**, 064301 (2003).
- [88] B. M. Terhal and G. Burkard, *Phys. Rev. A* **71**, 012336 (2005).
- [89] E. Novais and H. U. Baranger, *Phys. Rev. Lett.* **97**, 040501 (2006).
- [90] D. Aharonov, A. Kitaev, and J. Preskill, *Phys. Rev. Lett.* **96**, 050504 (2006).